Department of Physics and Astronomy

University of Heidelberg

Master thesis

in Physics

submitted by

Marcel Gutsche

born in Frankfurt am Main

2014

Surface Velocity Measurements

at the Aeolotron

by Means of Active Thermography

This Master thesis has been carried out by Marcel Gutsche

at the

Institute for Environmental Physics

under the supervision of

Prof. Dr. Bernd Jähne

and

Priv.-Doz. Dr. Christoph S. Garbe

Abstract

Abstract: This thesis presents measurements of the water velocity in the first few microns of the viscous boundary layer in the wind-wave facility Aeolotron by means of thermography. An active thermography method was used to create heat patterns, which were visualized by an infrared camera. In contrast to other methods, this approach is a non-invasive method and does not disturb the surface properties. Several algorithms are explored on synthetic sequences as well as on data taken at the Aeolotron to determine reliably surface velocities. In addition, the bulk velocity was measured using acoustic Doppler velocimetry (ADV). The momentum transfer resistance is determined by combining the bulk and the surface velocity at different wind speeds. The results contradict previous measurements based on trace gases, and therefore require further investigation.

Abstract, in deutscher Übersetzung: In dieser Arbeit wurde die Wassergeschwindigkeit in den obersten Mikrometern der viskosen Grenzschicht am Wind-Wellenkanal Aeolotron mit Hilfe von thermographischen Methoden gemessen. Unter Verwendung von aktiver Thermographie wurden Wärmemuster erzeugt, die mit einer Infrarotkamera vermessen wurden. Im Gegensatz zu anderen Messmethoden, ist dieser Ansatz nicht invasiv und beeinflusst damit nicht die Oberflächeneigenschaften. Verschiedene Algorithmen werden auf synthetischen Daten, als auch auf echten Daten von Experimenten am Aeolotron untersucht um verlässliche Geschwindigkeitsschätzungen zu ermitteln. Zusätzlich wurde die Bulkgeschwindigkeit mit Hilfe einer akustischen Strömungsmesssonde (ADV) gemessen. Der Impulstransferwiderstand wird für verschiedene Windgeschwindigkeiten bestimmt, indem man die Bulk-, sowie die Oberflächengeschwindigkeit zusammenführt. Die bei den Experimenten ermittelten Werte stehen im Widerspruch zu vorherigen Messungen, bei denen Gase als Tracer verwendet wurden, was weitere Untersuchungen notwendig macht.

Contents

1

Introduction

Since the beginning of the 20th century a steady increase in global mean temperatures is observed, which is mostly caused by anthropogenic factors such as the emission of green house gases [1]. The rise of temperature in the atmosphere and the oceans due to the amplified green house effect has a striking impact on the climate, which reflects the average pattern of temperature, precipitation and other meteorological variables over long periods of time. One of the many implications of higher average temperatures includes rising sea levels due to thermal expansion and the melting of glaciers and ice sheets. Also, droughts and severe weather will occur more frequently due to the accelerated water cycle [2, 3]. Due to the importance of the climate and its development in the next decades, the physical phenomena related to climate change are under strong investigation. The oceans act as a giant sink for the accumulated heat. They took up more than 90% of the additional heat introduced since 1971 [4]. The transport processes between the atmosphere and the sea play a key role for the development of the earth's climate and need to be known in greater detail. To acquire a better understanding of the transport mechanisms between the atmosphere and the oceans, the boundary between them must be investigated.

The air-sea interface is the bottleneck of heat transfer into the oceans. Close to the boundary layer the dominating transport mechanism for heat, momentum and gases is diffusion, which is a slow process on large scales. Important quantities which influence exchange processes at the interface are wind-induced shear stress [5] and the presence or absence of breaking waves [6]. These processes change the near-surface turbulence. The influence of these quantities on exchange processes is still not fully understood and remains an active field of research.

Flow fields are a valuable characteristic for describing the near surface turbulence and are of main interest for this thesis. Simulations show that there are strong correlations between the flow field and the exchange processes [7]. Several methods exist to measure the flow field. Particle image velocimetry (PIV) uses seeding particles to visualize the flow field [8, 9]. Other methods use thermography – images in the infrared regime of the water surface – to evaluate the flow fields. A distinction is made between passive [10] and active [11] thermography, where the latter refers to actively heated patterns on the water surface. Active thermography, therefore, provides superior signal strength at the cost of a more complex setup. This approach is used during this thesis, since it is a fast and an easy-to-apply method to investigate flow fields. It allows the study of the topmost layer – up to a few µm – in the velocity field, in contrast to PIV methods where the seeding particles are not constrained to the surface.

The thesis is structured in the following manner: first, the theoretical background governing the physical aspects of this thesis is presented. This includes in particular, the fluid dynamical description of shear currents and waves, and the principles of radiative transfer and thermography, which are used to investigate the surface flow. In the following chapter information on the measurement setup, including the wind-wave facility Aeolotron, the measurement devices and the conditions under which the flow is investigated, is provided. Thereafter, different image processing techniques which are used to evaluate the gathered image sequences are presented. Also, synthetic sequences which have been used to evaluate different algorithms for velocity estimation are introduced. Chapter 5 presents the results obtained with the synthetic sequences as well as the outcome of the experiments at the Aeolotron. Finally, the most important aspects of this thesis are summarized, an outlook for future work is given and improvements to the used setup are suggested.

2

Theory

In this chapter the theoretical foundations for this thesis is established. In a first part, the fluid dynamics relevant for the surface layer is discussed, which is of particular interest in this thesis. In the second part thermal radiation is addressed, the method of choice to investigate the surface dynamics.

2.1 Shear current and waves

This section describes the transport processes across interface boundaries and gives a brief introduction to some concepts of fluid dynamics which are relevant for this thesis. Detailed information regarding hydrodynamics can be found in [12, 13].

2.1.1 Transport processes

It must be distinguished between two different mechanisms of transport for momentum, heat and gases: the first one is turbulence, which is very efficient in transporting tracers over long distances. The second one is diffusion, which is a much slower process but dominates at the interface, since eddies – turbulent vortices – cannot penetrate the boundary layer. The diffusive layer close to the boundary has a thickness of 20 µm to 200 µm [14] on the waterside and it extends up to 1 cm on the air side.

To set a fluid in motion, momentum needs to be transfered into the water body. The transport of momentum was described by Newton as:

$$\tau_{ij} = \mu \frac{\partial \mathbf{v}_i}{\partial \mathbf{x}_j}, \tag{2.1}$$

where τ_{ij} describes the shear stress or the momentum flux, $\frac{\partial \mathbf{v}_i}{\partial \mathbf{x}_j}$ is the velocity gradient and μ is the dynamic viscosity of the fluid. The dynamic viscosity μ is related to the kinematic viscosity ν by

$$\mu = \nu\rho. \tag{2.2}$$

In analogy to eq. (2.1), the diffusive transport of mass can be described by Fick's law:

$$\mathbf{j} = -D\nabla c, \tag{2.3}$$

where $\mathbf{j}$ is the diffusion flux, D denotes the diffusion coefficient and c the concentration.

Again, in analogy to eq. (2.1) the conveyance of heat is given by Fourier's law:

$$\mathbf{q} = -\lambda\nabla T \tag{2.4}$$

with $\mathbf{q}$ as the heat flux density, λ is the conductivity of the given material.

The Navier-Stokes equation fully describes the dynamics of fluids – including turbulence – and is given for incompressible fluids by

$$\rho\left(\frac{\partial \mathbf{v}}{\partial t} + (\mathbf{v}\cdot\nabla)\,\mathbf{v}\right) = -\nabla p + \mu\Delta\mathbf{v} + \mathbf{f}, \tag{2.5}$$

where $\mathbf{f}$ is an external force per volume and p is the pressure. To predict the change from turbulent to laminar flow, the Reynolds number, defined as

$$Re = \frac{v\cdot d}{\nu}, \tag{2.6}$$

where d is the characteristic length of the geometry and v denotes the velocity, is used. For $Re > Re_{\text{crit}}$ a transition to turbulent flow is expected. To describe the turbulent effects, it is useful to separate the velocity into its time-averaged and fluctuating part:

$$u = \bar{u} + u' \tag{2.7}$$

where the fluctuating part u' vanishes if averaged over time. This procedure is also known as Reynolds decomposition. Applying the Reynolds decomposition to the stationary ($\frac{\partial \mathbf{v}}{\partial t} = 0$) Navier-Stokes equation (see eq. (2.5)), the Reynolds-averaged Navier–Stokes equations (RANS) is obtained:

$$\rho\bar{u}_j\frac{\partial \bar{u}_i}{\partial x_j} = -\frac{\partial \bar{p}}{\partial x_i} + \frac{\partial}{\partial x_j}\underbrace{\left[\mu\frac{\partial \bar{u}_i}{\partial x_j} + \rho\,\overline{u_i' u_j'}\right]}_{\tau_{ij}+\tau_{ij}'} + f_i, \tag{2.8}$$

where index notation is used. By taking the time average, the fluctuations are reduced to the Reynolds stress tensor $\rho\,\overline{u_i' u_j'} =: \tau_{ij}'$. Essentially, the fluctuations arising from the turbulence increase the effective viscosity. In analogy to eq. (2.1):

$$\tau_{ij,\text{tot}} = \tau_{ij} + \tau_{ij}' = \rho(\nu + K_i(x_j))\frac{\partial u_j}{\partial x_i}, \tag{2.9}$$

where $k_m = (\nu + K_i(x_j))$ represent a momentum transfer rate.

2.1.2 Boundary layer

Considering a flow along a boundary, such as a rigid wall, the water velocity will not be constant, but depend on the distance to the boundary due to the no-slip condition. It states that a viscus fluid has zero velocity at the boundary layer. This profile influences the transport of momentum, heat and chemical substances. In the following turbulent flow along a rigid wall is considered. A flow in the x-direction with the height-dependent velocity $u(y)$ is assumed. Introducing dimensionless quantities for generalization:

$$u^+ = \frac{u}{u_*} \quad \text{with} \quad u_*^2 = \frac{\tau_{\text{tot}}}{\rho} \tag{2.10}$$

$$y^+ = \frac{z}{z_*} \quad \text{with} \quad y_* = \frac{\nu}{u_*} \tag{2.11}$$

where u_* is the friction velocity and y_* is the thickness of the boundary layer. Close to the wall, where the flow is viscous, the relationship between the velocity and the distance from the wall is linear:

$$u^+ = y^+ \tag{2.12}$$

Farther away from the viscous boundary layer, the flow becomes turbulent, so we can neglect the viscous shear term $\tau_{ij} = \mu \frac{\partial u_j}{\partial x_i}$. The dominant term $\tau'_{ij} = \rho \overline{u'_i u'_j}$ can be approximated [15] as

$$\rho \overline{u'_i u'_j} \approx \rho (l \frac{\partial u}{\partial y})^2, \tag{2.13}$$

where l denotes the mixing length. The mixing length can be set to the height times a constant:

$$l = \kappa y. \tag{2.14}$$

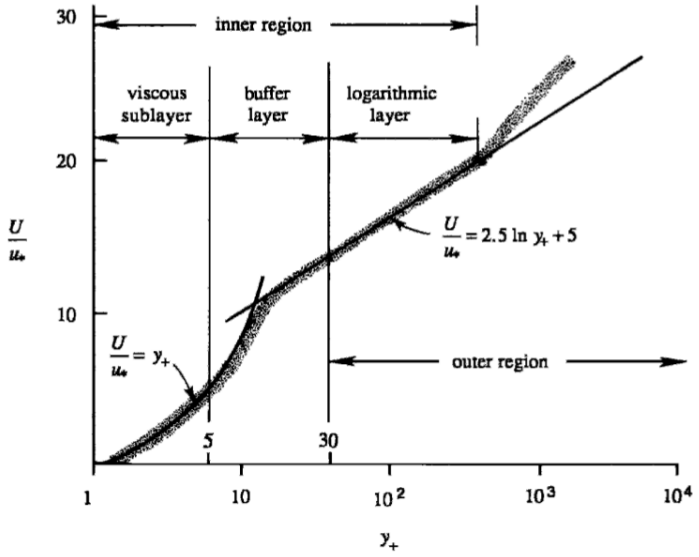

Figure 2.1.: Velocity profile in the vicinity of a rigid wall [13]. The shaded area represents a typical data cloud.

where κ refers to the Kármán constant κ is found to be $\kappa = 0.41$ [12]. For the turbulent case the shear velocity is found to be:

$$u_* = \kappa y \frac{\partial u}{\partial y} = u_* \kappa y^+ \frac{\partial u^+}{\partial y^+}. \tag{2.15}$$

Integrating eq. (2.15) yields the law of the wall:

$$u^+ = \frac{1}{\kappa} \ln\, y^+ + C^+, \tag{2.16}$$

where C^+ is an integration constant and is found to be 5 for a smooth wall (see fig. 2.1). In fig. 2.1 the transition from the linear to the logarithmic layer is shown. Both, the logarithmic behavior of eq. (2.16) and the linear regime following eq. (2.12) are clearly visible.

In fig. 2.2 a sketch of the velocity profile through the boundary layer is shown. When the total forces on the water body reached an equilibrium, the velocity in the bulk is assumed to be constant. Additionally, the viscous part of the shear stress is depicted, which increases from top to bottom, towards the boundary layer.

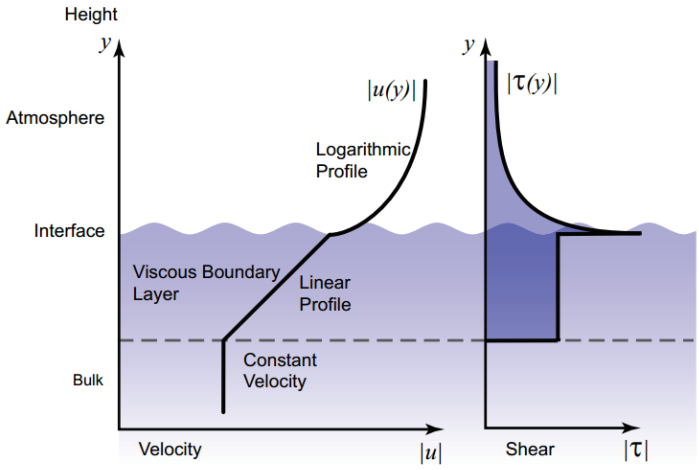

Figure 2.2.: Velocity profile through the boundary layer [16].

2.1.3 Schmidt number scaling

To quantify the gas exchange at the air-sea interface, tracers – gases or heat – are commonly used in experiments. To compare the transfer rates for different tracers one can utilize the so-called Schmidt number scaling.

$$\frac{k_1}{k_2} = \left(\frac{Sc_2}{Sc_1}\right)^n \tag{2.17}$$

where the Schmidt number is introduced which is defined as $Sc = \frac{\nu}{D}$. The Schmidt number exponent n lies between $\frac{2}{3}$ for a flat surface and $\frac{1}{2}$ for a wavy, rough surface. Relating the transfer velocity to the momentum transport, the following relation can be found [17, 18]:

$$k = \frac{1}{\beta} u_* Sc^{-n} \tag{2.18}$$

where β is a dimensionless constant. For the momentum transfer velocity this reduces to

$$k_m = \frac{1}{\beta} u_*. \tag{2.19}$$

2.1.4 Orbital motion and waves

Waves at the water surface directly influence the dynamics of the air water-system. They also alter the perceived surface velocity by their altitude and the underlying orbital motion. Therefore, some important quantities to characterize the wave field are discussed.

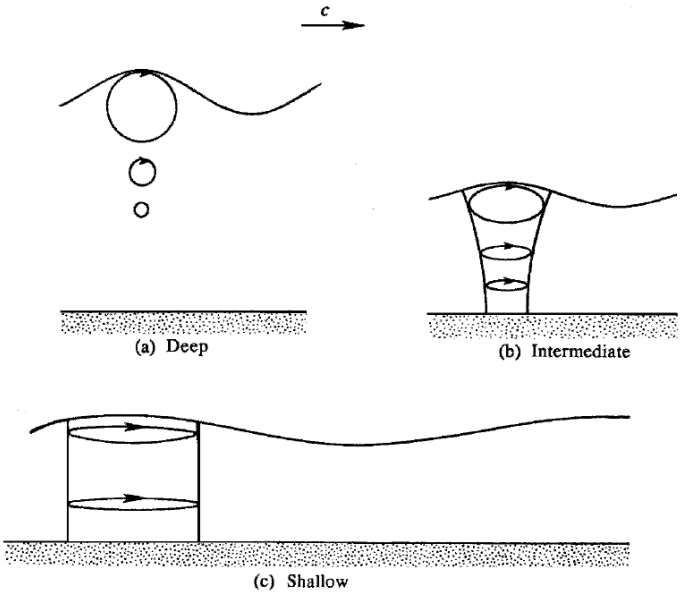

Figure 2.3.: Orbital motion for gravity waves [13]. Depicted are three different depths, where a transition from circular to ellipsoidal orbital motion takes place with decreasing depth.

The orbital motions of gravity waves (wavelengths $\lambda > 10\,\mathrm{cm}$) are described by linear wave theory, assuming that the wave amplitude A is small in comparison to the water depth h and the wavelength λ. Considering the propagation of a wave (see fig. 2.3 for reference) in x-direction with water velocity components u and w, depending on the deepness z and the wave height η, the solution for the equations of motion are described by [13]

$$u(x,z,t) = A\omega \frac{\cosh(k(z+h))}{\sinh(kh)} \cos(kx - \omega t) \tag{2.20}$$

$$w(x,z,t) = A\omega \frac{\cosh(k(z+h))}{\sinh(kh)} \sin(kx - \omega t) \tag{2.21}$$

$$\eta(x,t) = Ag \cos(kx - \omega t). \tag{2.22}$$

Here k denotes the wave number, ω the frequency and g is the local gravitational acceleration. The dispersion relation is given by

$$c = \frac{\omega}{k} = \sqrt{\frac{g}{k} \tanh(kh)}, \tag{2.23}$$

which can be used to derive the total energy, the sum of potential and kinetic energy:

$$E = \rho g \overline{\eta^2} = \frac{1}{2} \rho g A^2 \tag{2.24}$$

with $\overline{\eta^2}$ describing the time-averaged quadratic deflection.

2.2 Thermography

Thermography refers to imaging techniques utilizing infrared radiation, where we can relate the measured intensity to a temperature. Invisible for the human eye, thermal radiation provides insightful information of objects which are more difficult to study in the visible spectrum, e.g. in the infrared specular reflections at the water surface can be avoided.

2.2.1 Heat transport

In addition to the transport mechanisms of momentum and substances, heat can also be transported via radiation. In total, it can be differentiated between three types of thermal transport: conduction, convection and radiation. Thermal conduction transports kinetic energy between neighboring atoms or molecules by collisions and is described by eq. (2.4). Convectional transport is due to density gradients in a gravitational potential, where the buoyancy force affects large regions of the fluid and enforces an upwards motion which carries the heat with it. Attention should be paid to the fact that conduction transports energy without material exchange which is the case in convection.

Similar to conduction, thermal radiation transfers energy without material exchange, over large distance via an electromagnetic field. This is explained in more detail in the next section. It is common in environmental science to distinguish between latent and sensible heat, where latent heat refers to an energy transfer between two systems while having constant temperature, usually during a phase transition, e.g. the melting of ice. In contrast, sensible heat is exchange of heat under a change of temperature and can be measured with a thermometer.

2.2.2 Thermal radiation

The emission spectrum of a black body is governed by Planck's law:

$$I_\lambda(T) = \frac{2hc^2}{\lambda^5} \frac{1}{e^{\frac{hc}{\lambda k_\mathrm{B} T}} - 1} \tag{2.25}$$

where I is the spectral radiance, Planck's constant h, the speed of light c, Boltzmann's constant k_B, the Temperature T and the wavelength λ. It can also be formulated in dependence of the frequency ν:

$$I_\nu(T) = \frac{2h\nu^3}{c^2} \frac{1}{e^{\frac{h\nu}{k_\mathrm{B} T}} - 1}. \tag{2.26}$$

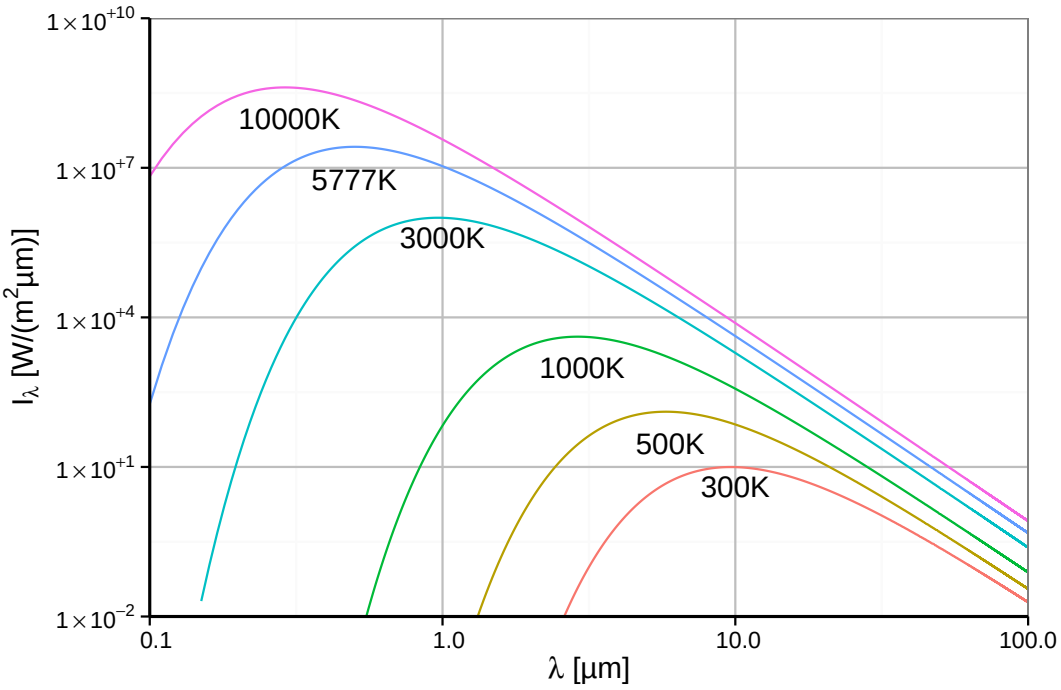

Figure 2.4.: Blackbody spectra for several temperatures on a log-log scale.

Electromagnetic waves with wavelengths between 700 nm and 1 mm are usually referred to as the infrared regime. In fig. 2.4 Planck's law for different temperatures is given. The total energy emission increases with temperature and a shift of the maximum of the spectrum towards lower wavelengths can be noticed. This is governed by Wien's displacement law:

$$\lambda_{\max} T = 2.898 \times 10^{-3}\,\mathrm{m\,K} \tag{2.27}$$

Integrating eq. (2.25) over all wavelengths yields the Stefan–Boltzmann law:

$$L = \sigma T^4 \tag{2.28}$$

where L is the power P per area A and the Stefan-Boltzmann constant $\sigma = 5.67 \times 10^{-8}\,\mathrm{W/m^2/K^{-4}}$.

2.2.3 Properties of the water surface in the infrared

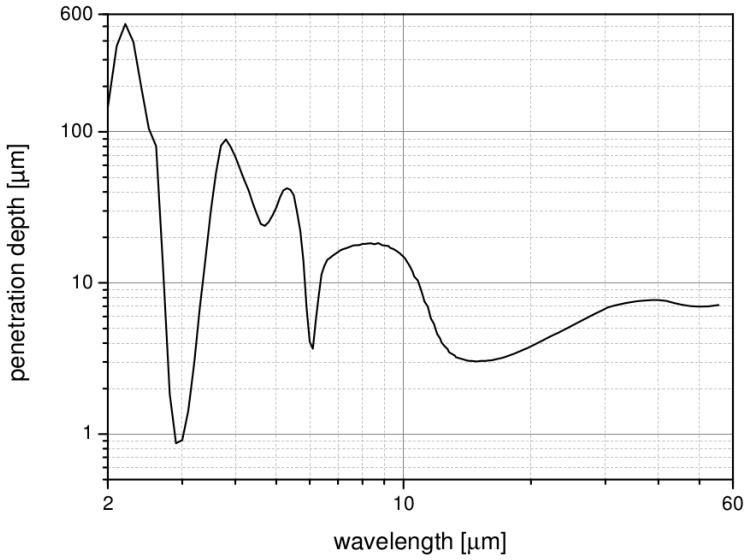

Figure 2.5.: Penetration depth of the electromagnetic radiation in the infrared regime in water [19].

In fig. 2.5 the penetration depth for different wavelengths in the infrared is shown. Electromagnetic waves with a wavelength between 2–60 µm can penetrate the water surface up to 600 µm. Since water is transparent in the visible regime, it is difficult to explore the surface boundary with a normal camera setup. Therefore, it is advantageous to examine the water surface in the infrared, where it is opaque and reflections and specularities are reduced.

3

Measurement setup

In this chapter the wind wave facility Aeolotron is described, where the measurements took place, and the measurement technique used to capture infrared image sequences of the water surface is explained. Afterwards, active thermography is introduced, which is used to determine surface velocities. Therefore, a carbon dioxide laser is used, which generates a heat pattern on the water surface. Afterwards, the conditions under which the measurements have been carried out are presented.

3.1 Wind-wave facility Aeolotron

The annular wind-wave facility Aeolotron constructed in 1999 in Heidelberg has an outer diameter of 10 m, a flume width of 60 cm and total height of 2.4 m. Filling it up to 1 m with deionized water results in a water volume of 18 000 l. The wind is generated by two axial fans, which can provide a reference wind speed up to $10.5\,\mathrm{m\,s^{-1}}$. The axial fans are controlled via a drive frequency ν

given in Hz. In table 3.1 frequencies and corresponding wind speeds, which are used for the experiments during this thesis, are shown [20].

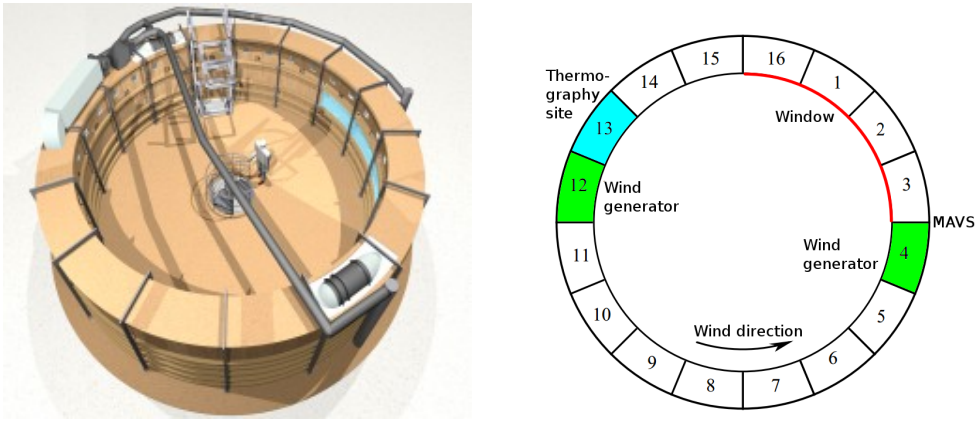

Figure 3.1.: On the left hand side a rendered view of the Aeolotron is shown [21]. The Aeolotron is divided in 16 segments. The thermography site is located at segment 13, whereas the MAVS device for measuring the bulk velocity is placed between segment 3 and 4 (image on the right based on [22]).

Due to the annular shape of the Aeolotron – and therefore, the virtually unlimited fetch – the wind transports momentum into the water body until a stationary equilibrium is reached. This is a great advantage over more common, linear facilities, which have a limited fetch. This fetch limitation makes it more difficult to compare results of measurements with data measured on the ocean. But the annular shape is at the same time a drawback. Due to the circular path of the air and the water motion, centrifugal forces act on the water and air body. This alters the air flow and prevents the development of a logarithmic wind profile.

The facility is chemically inert, which means that experiments can be run with sea water if desired. It is also thermally isolated, a reflective foil prevents thermal loss by radiation. Thus, the annular shaped Aeolotron is a favorable experimental site to conduct experiments concerning exchange rates of heat, momentum and chemical tracers.

3.2 Active thermography

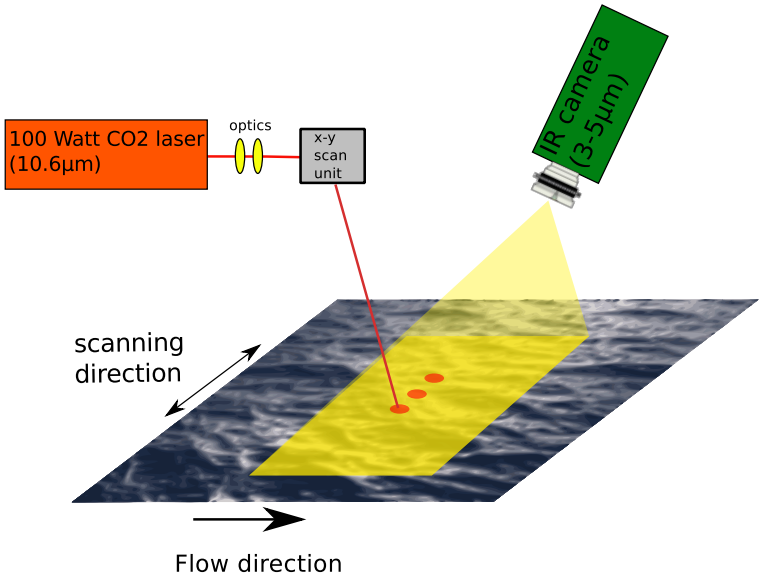

Figure 3.2.: Sketch of the thermography measurement setup. The yellow area is the field of view of the infrared camera. The red dots are thermal marker, "drawn" by the carbon dioxide laser.

In fig. 3.2 a sketch of the measurement setup is shown. A carbon dioxide laser emitting infrared radiation at a wavelength of 10.6 µm with a Gaussian intensity profile is used in this thesis. The laser beam is deflected using a scanning unit, which consists of two rotating, electronically controlled mirrors. A row of points is heated by 0.5–1.0 K (marked in red) perpendicular to the wind direction on the water surface. An actively cooled infrared camera, which is sensitive in the range of 3–5 µm and has a resolution of 640x512 pixels, detects the heat signature. The field of view – marked in yellow – has a size of 46.7 cm × 37.4 cm, which corresponds to a scale factor of 0.73 mm/pixel.

To avoid reflections from the cooled camera sensor in the IR image, the camera is inclined at an angle of about 15° to the surface normal. For the measurements presented here a lens with a focal length of $f = 50$ mm is used. Images are taken with 120 frames per second with an integration time of 2.5 ms. Due to this fast capturing speed, it is possible to keep the location shift between consecutive images small (less than one pixel), which is beneficial for the subsequent image processing steps.

Figure 3.3.: Example image at $1.52\,\mathrm{m\,s^{-1}}$ wind generator frequency from an IR sequence, which is inverted for better visibility. Darker colors correspond to higher temperature. The heated spot at the bottom has been drawn in the current frame. The flow is directed to the left. Dead pixels have been removed using a median filter.

The CO_2 laser has a output power of 125 W which is continuously adjustable and works in a pulsed mode with a frequency of 5 kHz. The laser beam has a diameter of about 8 mm after it was widened by a Keplerian telescope to prevent damage to the scanner system. With this setup, the surface temperature can be increased by up to 5 °C and therefore could induce a stable stratification, which is undesirable in many applications. However, this had no impact on the measured surface velocity, which was experimentally verified. The only limiting factor for the energy deposition was an effect which occurred due to the fast evaporation at the water surface. Thus, concentric circles emerge from the center of the heated dots, if the laser power was set too high. Hence, the maximum laser power available could not be used, which would have been advantageous for a high signal-to-noise ratio. The signal-to-noise ratio in this context is defined as

$$\mathrm{SNR} = \frac{I_{max} - I_{bg}}{\sigma_{bg}} \tag{3.1}$$

where I_{max} is the maximum signal intensity of the heat patch, I_{bg} is the average intensity of the background and σ_{bg} is the standard deviation of the intensity of the background pixels.

By synchronizing the camera, the scanning unit and the laser well defined thermal markers could be drawn onto the water surface and could be captured when the intensity is at a maximum (see fig. 3.3). Instead of a point pattern, also a line could be drawn on the surface. However, that would lead to a loss of information about the velocity component perpendicular to the line. More technical details of the used equipment can be found in the appendix.

3.3 Bulk velocity measurement

To measure the velocity in the water bulk an acoustic flow measurement device is used, which is permanently installed in the Aeolotron wind wave tank. The device in use is a MAVS-3 (Modular Acoustic Velocity Sensor) manufactured by Nobska which measures the running time of acoustic signals. By using the Doppler effect the MAVS-3 can measure the bulk velocity in all three dimensions. The device uses four axes for measuring the velocity components. The fourth axis is used to increase the accuracy. The device is located 50 cm below the water surface with the probe head in the center of the flume. It provides velocities with a time resolution of 20 Hz. Further information on the MAVS-3 can be found in [23].

3.4 Measurement conditions

All measurements have been carried out at the wind wave facility Aeolotron using clean, deionized water. After starting the wind engine the system needs time to reach an equilibrium indicated by a constant water bulk velocity over several minutes. For low wind speeds, reaching this equilibrium took up to 1.5 hours. For the first eight frames heated dots were drawn onto the water surface in a distance of 4.5 cm to each other. After 104 frames another set of eight

points was induced onto the surface. This avoided overpopulating the surface with dots, which would make an analysis more difficult. An overview of the measurement conditions is given in table 3.1. The preliminary u_{10} values shown here were calculated by [20] using the parameterization proposed by [24]. The u_{10} value describes the wind speed in 10 m above the water surface and is a common parameter to compare measurements from the ocean with laboratory experiments.

Drive frequency ν [Hz]	Laser power [%]	u_{ref} [$\mathrm{m\,s^{-1}}$]	u_{10} [$\mathrm{m\,s^{-1}}$]
5	2	1.52	1.81
9	2	2.79	3.88
16	2	5.08	6.73
22	4	6.72	9.65

Table 3.1.: Overview of the measurement conditions for the experiments in the Aeolotron. The preliminary wind speeds in the Aeolotron are given by [20]. u_{ref} is the reference wind speed at the Aeolotron which is measured using a pitot tube. The laser power could be adjusted as a percentage of the maximum output.

Although, the experiments are carried out with clean water, the development of surface films cannot be suppressed entirely. This leads to wave damping and therefore a different behavior in the air-sea interaction.

4

Methods

In this chapter the methods used to analyze and evaluate the image sequences captured by the infrared camera are discussed. The first part deals with general image processing tasks. In the second part, velocity estimation algorithms used in this thesis are presented. The third part will illustrate how to generate synthetic sequences to provide realistic ground truth – image, where the exact locations and velocities of the heated dots are known – with respect to the given setting of localized, shape deforming blobs with a high signal-to-noise-ratio moving on a mostly uniform illuminated surface.

4.1 Image processing

Image processing is a still growing field in the domain of computer science and uses algorithms to manipulate and analyze images. Common tasks in image processing include feature detection, e.g. edges or corners, and segmentation to distinguish between objects of interest and the background. In this thesis image

processing is used to determine velocities in image sequences captured with an infrared camera. The generation of these sequences was described in section 3.2 and a typical image is given in fig. 3.3. The objects of interest are small, heated dots with a diameter of approximately 10 pixels and are far apart from each other. To infer velocities from these markers over consecutive frames, the heated dots are separated from the background using segmentation. Afterwards, features, which aid in velocity estimation are extracted.

4.1.1 Segmentation

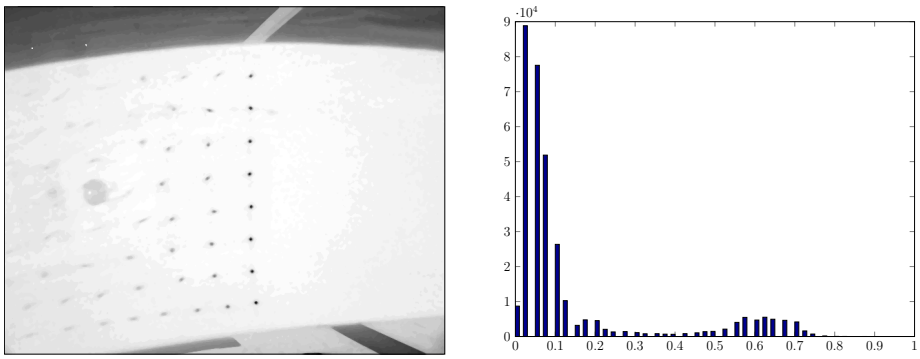

Figure 4.1.: Infrared image of the water surface on the left hand side. The image is inverted for better visibility, meaning that a lower intensity corresponds to higher temperature. The flow direction is from the right to the left. On the right hand side, the corresponding histogram with a bi-modal distribution is shown.

To extract certain parameters from image sequences, preprocessing methods are used to separate the signal of interest – in this thesis heated dots on a water surface – from noise or clutter. The result is a binary image, where pixels belonging to a heated dot have a value of one and the background has a value of zero. There are plenty methods available to perform this task, e.g. simple discrimination by thresholding [25, 26], using contour edges to separate objects [27], region growth methods [28] and – taking temporal information into account – Gaussian mixture models [29], to name just a few. In this thesis Otsu's method – a threshold based segmentation approach – and an edge detection method are used to segment the image. Otsu's method determines the threshold by minimizing the variance within the class, assuming that the image has a bi-modal histogram (see fig. 4.1). For edge detection the Canny edge detector is used. It

involves several steps which are briefly outlined, since some concepts are relevant throughout this chapter. A detailed explanation of the Canny detector can be found in [30].

The canny edge detector consists of several steps. In a first step the image is convolved with a Gaussian filter to blur the image and suppress noise, which could lead to falsely classified edges. A convolution with an approximation of a 5x5 Gaussian filter with a standard deviation $\sigma = 1$ would be described by

$$\mathbf{I}_{\text{blurred}} = \frac{1}{337}\begin{bmatrix} 1 & 4 & 7 & 4 & 1 \\ 4 & 20 & 33 & 20 & 4 \\ 7 & 33 & 55 & 33 & 7 \\ 4 & 20 & 33 & 20 & 4 \\ 1 & 4 & 7 & 4 & 1 \end{bmatrix} * \mathbf{I}_{\text{raw}}, \tag{4.1}$$

where the asterisks denotes a convolution, which is defined in one dimension for continuous functions $f(t)$ and $g(t)$ as

$$(f * g)(t) = \int_{-\infty}^{\infty} f(\tau)\, g(t - \tau)\, d\tau. \tag{4.2}$$

An edge is perceived as a fast change in intensity values over adjacent pixels. Hence, in a second step, the gradient along the x and y-direction of the image contains crucial information about the edges. An estimate for the image gradients $\mathbf{I}_x$ and $\mathbf{I}_y$ can be approximated by using the Sobel kernel:

$$\mathbf{I}_x = \begin{bmatrix} -1 & 0 & +1 \\ -2 & 0 & +2 \\ -1 & 0 & +1 \end{bmatrix} * \mathbf{I} \quad \text{and} \quad \mathbf{I}_y = \begin{bmatrix} +1 & +2 & +1 \\ 0 & 0 & 0 \\ -1 & -2 & -1 \end{bmatrix} * \mathbf{I} \tag{4.3}$$

The absolute magnitude and direction, of the gradient can then be computed by

$$\mathbf{G} = \sqrt{\mathbf{I}_x{}^2 + \mathbf{I}_y{}^2} \tag{4.4}$$

$$\mathbf{\Theta} = \operatorname{atan2}\left(\mathbf{I}_y, \mathbf{I}_x\right), \tag{4.5}$$

where atan2 is the arctangent function with two arguments. Since each pixel has only 8 neighbors, the edge direction $\mathbf{\Theta}$ is rounded to 0°, 45°, 90° and 135°. To ensure that the edge has a width of no more than a pixel, the edges are thinned out using non-maximum suppression, in a following step. Thereby, each pixel is set to zero, if its value is not greater than its neighbors in gradient direction. In a last step, a process called hysteresis thresholding is applied to avoid discontinuities in the edge due to a varying gradient strength. Therefore, two thresholds are used, a high and a low one. Using the high threshold, starting points for edges can be chosen with high confidence. Using the gradient direction, these starting points are utilized to trace along the edge, now using the lower threshold to preserve faint details. After this last step, the algorithm terminates and the edges can then be used to separate objects from the background using the edge as a boundary.

Both techniques are used in this thesis. The simple threshold approach based on Otsu's method is fast and reliable when the signal-to-noise-ratio is high (SNR > 50). For images where the SNR of the heated dots was less than 50, the segmentation technique based on the Canny edge detector was used, which was slower in terms of computation speed, but returned reliable results in the presence of noise. After the segmentation stage an additional step involves to connect the pixels which form a connected region and attach a label to each. Algorithms to do so were proposed by [31, 32]. Thereafter, a variety of features could be extracted from these connected components which represent the heated dots.

4.1.2 Feature detection

Image features play an important role in classification tasks, such as discriminating between different kinds of plant seeds in an image. In this thesis features such as the area of a heated dot, or their circularity are used to estimate the reliability for velocity estimation. To calculate the speed of a heated spot, one central feature is the exact location on a sub-pixel scale. This is explained in more detail in section 4.2.4. Other useful quantities, to estimate the reliability of the measured signal are the maximum intensity $I_{\max}$, the area A and the circularity c. The circularity c is defined in this thesis as

$$c = \frac{4\pi A}{U^2}, \tag{4.6}$$

where U is the perimeter of the heated dot.

4.2 Velocity estimation algorithms

To determine which technique is best suited for extracting velocity information from the captured infrared sequences – in terms of computation speed and accuracy – several methods have been tested. The basic principles of each will be presented in the following sections.

4.2.1 Hough transform

To infer velocities from image sequences, it can be useful to stack the images along the time axis. Slices from the $x\,t$ or $y\,t$-plane – also called spatio-temporal images – contain velocity information in the slope of the emerging structures (see fig. 4.2). For a constant motion the structures in the spatio-temporal image are straight lines. The slope of these lines corresponds to the velocity of the object in the image. To detect lines the Hough transform [33] can be utilized. A line can be parametrized by

$$y = mx + b, \tag{4.7}$$

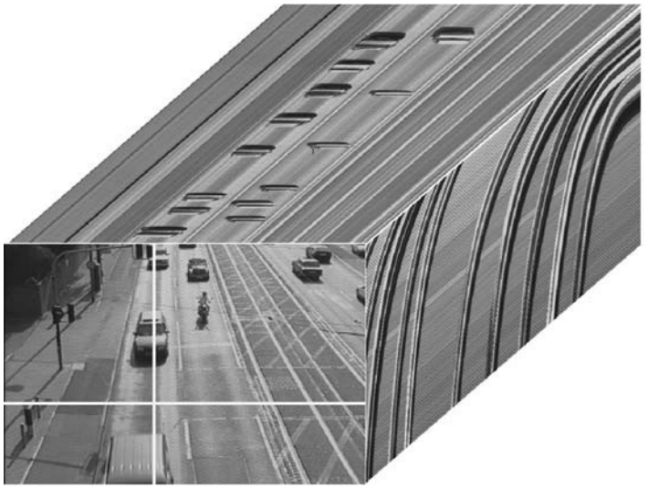

Figure 4.2.: Images are stacked along the time axis. On the right side a $y\,t$-slice from the vertical white line in the image is shown, whereas the top of the cube shows a $x\,t$-slice form the horizontal line. The slopes in the $x\,t$ and $y\,t$ corresponds to the velocities of objects passing through these lines [27].

where x and y are the image coordinates, and m – the slope of the line – and b – the offset to the origin – are the parameters. So each line can be presented by their parameters m and b. However, a problem posed by this parametrization are vertical lines, where the slope becomes infinity. Using the Hesse normal form

$$y = -x\frac{\cos\theta}{\sin\theta} + \frac{d}{sin\theta}, \tag{4.8}$$

where the parameters are the angle θ and the distance from the origin d, the parameter space remains finite. Considering the parameters for all possible lines going through a point (x_0, y_0) in the image, their representation in the parameter space – also called Hough space – would correspond to a sinusoidal curve. Considering a second point (x_1, y_1), the representation of both points would cross in the Hough space, where a line in the image space goes through both points. The hough approach is a voting based method, since each pixel votes with its gray value for a set of parameters in the hough space [27].

Peaks in the Hough space correspond to lines in the spatial domain (see fig. 4.3), so that detecting lines simplifies to finding local maxima in the Hough space. As discussed above, the Hough transform can be utilized when taking slices from

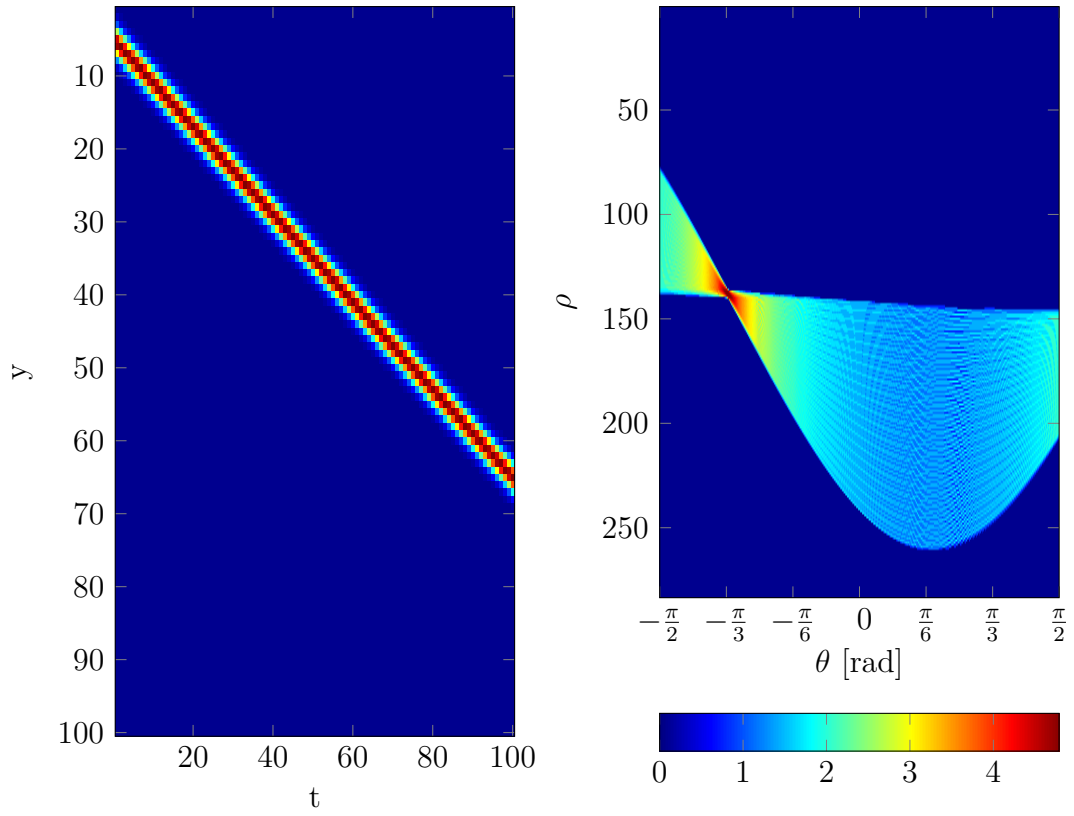

Figure 4.3.: Hough detection of a straight line in the $y\,t$-plane. On the left hand side the spatial space is visualized and on the right hand side the hough transform (with logarithmic intensity values for visibility) is shown.

the $x\,t$ or $y\,t$-plane in the infrared sequences. Assuming a constant motion, then only the slope of the line is needed to determine the velocity. So basically,

$$v = -\cot(\theta) \tag{4.9}$$

sticking to the previously introduced notation. Of course, this approach will break down if the motion is non-uniform.

4.2.2 Optical flow

The apparent motion of an object in a visual system is called optical flow. This concept was first implemented by Horn and Schunck in 1981 [34]. The fundamental assumption of optical flow algorithms is the brightness constancy

$$\frac{\mathrm{d}I}{\mathrm{d}t} = \frac{\partial I}{\partial t} + \frac{\partial I}{\partial x}\frac{\mathrm{d}x}{\mathrm{d}t} + \frac{\partial I}{\partial y}\frac{\mathrm{d}y}{\mathrm{d}t} = 0 \tag{4.10}$$

which can also be written as

$$I_x u + I_y v + I_t = 0 \tag{4.11}$$

where I_x, I_y and I_t denote the derivatives with respect to x, y and t. The velocity components u and v are in x and y-direction. This means, that the overall intensity stays constant over space and time. This assumption seems preposterous, since occlusions, appearance and disappearance of objects are usual events in an image sequences. However, it is a good starting point to elaborate more sophisticated approaches on an initial guess. There is one equation with two unknowns, so additional boundary conditions are needed to solve for the velocity components u and v. This lack of information is also known as the aperture problem. The next paragraphs present two common methods of an optical flow implementation.

Horn-Schunck algorithm

The Horn-Schunck approach assumes global smoothness as a second constraint for the optical flow. This means, that there are no sudden changes in the velocity field. To find an optimal solution which satisfies the smoothness-constraint as well as the brightness constancy assumption, the Horn-Schunck algorithm minimizes the functional

$$E = \iint \underbrace{\left[(I_x u + I_y v + I_t)^2 + \alpha^2(\|\nabla u\|^2 + \|\nabla v\|^2)\right]}_{:=L} \mathrm{d}x\mathrm{d}y. \tag{4.12}$$

This expression relates the brightness constancy term $I_x u + I_y v + I_t$ and the smoothness constraint $\|\nabla u\|^2 + \|\nabla v\|^2$ to the global energy E, where α tunes the smoothness constraint in comparison with the brightness constancy. The global energy is minimized, hence the velocity field must conform to the brightness constancy assumption and the velocity field gradients should be minimal.

Using the related Euler-Lagrange equations this functional can be minimized. The Euler-Lagrange equation are given by

$$\frac{\partial L}{\partial u} - \frac{\partial}{\partial x}\frac{\partial L}{\partial u_x} - \frac{\partial}{\partial y}\frac{\partial L}{\partial u_y} = 0 \tag{4.13}$$

$$\frac{\partial L}{\partial v} - \frac{\partial}{\partial x}\frac{\partial L}{\partial v_x} - \frac{\partial}{\partial y}\frac{\partial L}{\partial v_y} = 0 \tag{4.14}$$

and inserting yields

$$I_x(I_x u + I_y v + I_t) - \alpha^2 \Delta u = 0 \tag{4.15}$$

$$I_y(I_x u + I_y v + I_t) - \alpha^2 \Delta v = 0. \tag{4.16}$$

The Laplacian Δu can be approximated by

$$\Delta u(x, y) = \bar{u}(x, y) - u(x, y) \tag{4.17}$$

where $\bar{u}$ is weighted averaged in a local neighborhood around (x, y). Since the coupled equation depends on the local neighborhood in the flow field, the equation once $\bar{u}$ and $\bar{v}$ have been calculated must be updated. The following update scheme is established:

$$u^{k+1} = \overline{u}^k - \frac{I_x(I_x\overline{u}^k + I_y\overline{v}^k + I_t)}{\alpha^2 + I_x^2 + I_y^2} \tag{4.18}$$

$$v^{k+1} = \overline{v}^k - \frac{I_y(I_x\overline{u}^k + I_y\overline{v}^k + I_t)}{\alpha^2 + I_x^2 + I_y^2} \tag{4.19}$$

If there is no better initial estimate for the flow field it is usually set to zero. During this thesis, the abbreviation HS is used to refer to the approach discussed above.

Lukas-Kanade algorithm

In contrary to the Horn-Schunck approach – which is a global method, meaning that all pixels contribute to the velocity field – the Lukas-Kanade algorithm acts only on a local neighborhood of pixels. To provide additional equations in addition to eq. (4.10) it is assumed that pixels within a certain window around a point p must have the same velocity. This gives a set of equations

$$\begin{aligned} I_x(q_1)V_x + I_y(q_1)V_y &= -I_t(q_1) \\ I_x(q_2)V_x + I_y(q_2)V_y &= -I_t(q_2) \\ &\vdots \\ I_x(q_n)V_x + I_y(q_n)V_y &= -I_t(q_n) \end{aligned} \tag{4.20}$$

where q are points in the neighborhood of p. This over-determined equation system can be solved by least square methods.

The Horn-Schunck approach is especially useful in sceneries were large portions of the image are moved, e.g. when the camera is panned. Then, occlusions are not a dominant contribution. It generally provides dense flow fields, since the smoothness constraint fills in information from the neighborhood. The iterative procedure of the Horn-Schunck method is a bottleneck in computation

speed. The Lukas-Kanade approach on the other hand, is more robust with inconsistencies in the global flow field, e.g. occlusions that can occur. However, it lacks the ability to provide dense flow fields. In this thesis, there is only local information about the velocity field, where heated dots are present on the water surface. Thus, it is to be expected that the Horn-Schunck algorithm provides less accurate velocity estimations than the Lukas-Kanade approach. In the following, sometimes the term LK is used to refer to the above explained algorithm.

4.2.3 Discrete Fourier transformation for image matching

Considering only rigid translation of objects in an image sequence the cross-correlation can be exploited, which is a measure of similarity for two signals $f(t)$ and $g(t)$. For a 1D signal the cross-correlation $f \star g$ is defined as

$$(f \star g)(\tau) = \int_{-\infty}^{\infty} f^*(t)\ g(t+\tau)\,\mathrm{d}t, \tag{4.21}$$

where f^* is the complex conjugate of f. The cross-correlation is related to the convolution by

$$(f \star g)(\tau) = f^*(-\tau) * g(\tau), \tag{4.22}$$

where the convolution is by eq. (4.22).

Given two images $\mathbf{I}_1$ and $\mathbf{I}_2$, and assuming that both only differ by a small displacement which can be expressed as a rigid translation, e.g. $\mathbf{I}_1(\mathbf{x}) = \mathbf{I}_2(\mathbf{x}') = \mathbf{I}_2(\mathbf{x} + \Delta\mathbf{x})$, the translational vector can be found by searching for the maximum in the cross-correlation ($\frac{\partial \mathbf{C}}{\partial \mathbf{x}'} = 0$ for $\mathbf{x}' = \Delta\mathbf{x}$) . Calculating the cross-correlation of a 2D signal leads to

$$\mathbf{C}(\mathbf{x}') = \iint_{-\infty}^{\infty} \mathbf{I}_1^*(\mathbf{x})\mathbf{I}_2(\mathbf{x}+\mathbf{x}')\,\mathrm{d}\mathbf{x} \tag{4.23}$$

where $\mathbf{I}_1^*$ denotes the complex-conjugate of $\mathbf{I}_1$. This operation is related to a convolution via eq. (4.22) and therefore it can be efficiently calculated in the Fourier space using the convolution theorem

$$\mathbf{C}(\mathbf{x}') = \mathbf{I}_1^*(-\mathbf{x}') * \mathbf{I}_2(\mathbf{x}') = \mathcal{F}^{-1}\left[\mathcal{F}(\mathbf{I}_1^*(-\mathbf{x}')) \cdot \mathcal{F}(\mathbf{I}_2(\mathbf{x}'))\right]. \tag{4.24}$$

The discrete Fourier transformation in two dimensions is given by:

$$\hat{a}_{k,l} = \sum_{m=0}^{M-1} \sum_{n=0}^{N-1} a_{m,n} \cdot \mathrm{e}^{-2\pi \mathrm{i} \cdot \frac{mk}{M}} \mathrm{e}^{-2\pi \mathrm{i} \cdot \frac{nl}{N}}, \tag{4.25}$$

where M and N describe the image dimensions.

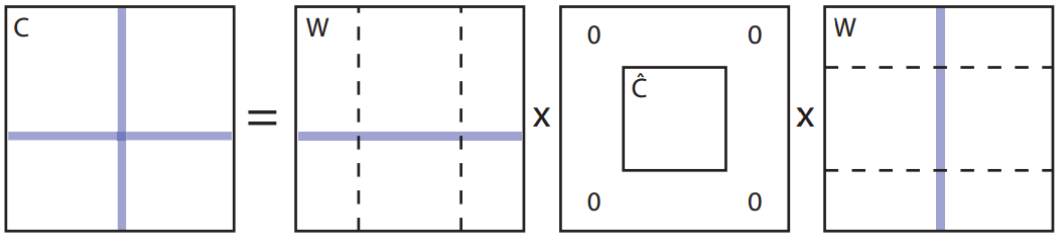

Figure 4.4.: Illustration of the procedure for fast subpixel image registration by cross correlation (figure taken from [35]).

To achieve sub pixel accuracy the usual approach is to zero-pad the Fourier transform image so that an up sampled array of a factor depending on the desired sub pixel resolution (e.g. 2x2 for 0.5 pixels in accuracy) is achieved. These up-sampled images can get very large and are therefore difficult to process on common computers. An efficient approach to circumvent these issues was proposed by [36]. Instead of computing the cross correlation by means of fast Fourier Transform (FFT) algorithm a matrix multiplication can be used, where the inverse discrete 2D Fourier transform is given by

$$C = \mathbf{W_N}\, \hat{C}\, \mathbf{W_N} \tag{4.26}$$

with $\mathbf{W_N}$ being an $N \times N$ Matrix with the following entries

$$\mathbf{W_N^{j,k}} = \frac{1}{\sqrt{N}} \exp\left(2\pi i(j \cdot k)/N\right) \tag{4.27}$$

Knowing the maximum of the cross correlation to pixel precision, which can be done efficiently in the Fourier domain, only the up-sampled version needs to be evaluated in a small neighborhood in the vicinity of the peak. This procedure is illustrated in fig. 4.4 and explained in more detail in [35]. In the following, this algorithm is sometimes abbreviated as DFT.

4.2.4 Tracking

Tracking means to trace the movement of an object over time. Hence, it is not only possible to retrieve velocities, but also to track the history of individual objects, allowing differentiated evaluation of statistical properties in hydrodynamic systems. The objects which are dealt with are heated dots with a Gaussian intensity distribution. Besides the position and velocity of the heated dots, several properties, such as the intensity, the signal-to-noise-ratio and the area – to mention just a few – are evaluated and saved to the record of each track. The track record is basically a list, where all information about the tracked object is saved to.

The following approach is based on a MATLAB example [37], which keeps track of each detected object. The complete outline of the tracking method is depicted in fig. 4.5. First, the image is segmented in a foreground and background area, by means of Otsu's method for a high signal-to-noise-ratio (SNR > 50) or by means of an edge based segmentation procedure for low SNR, as described in section 4.1.1. For edge detection the Canny edge detector is used.

After the segmentation stage, connected pixels are labeled as separate regions. These regions represent the detected heated dots in the image and are also used as a starting point for the optical flow algorithms as well as the DFT approach. To reduce computation time sub-images around the located spots of interest are passed to the above mentioned algorithms.

For each detected region, the centroid on the gray value image is computed by

$$\mathbf{x} = \frac{\sum\limits_{k\in\Omega} \mathbf{I}_k \mathbf{x}_k}{\sum\limits_{k\in\Omega} \mathbf{I}_k}, \tag{4.28}$$

where Ω is the isolated region which has been identified by the segmentation, $\mathbf{x}_k$ is the discrete pixel location and $\mathbf{I}_k$ the intensity at that location. The centroid is the sub-pixel location of the intensity peak and therefore a very important quantity to infer velocities from.

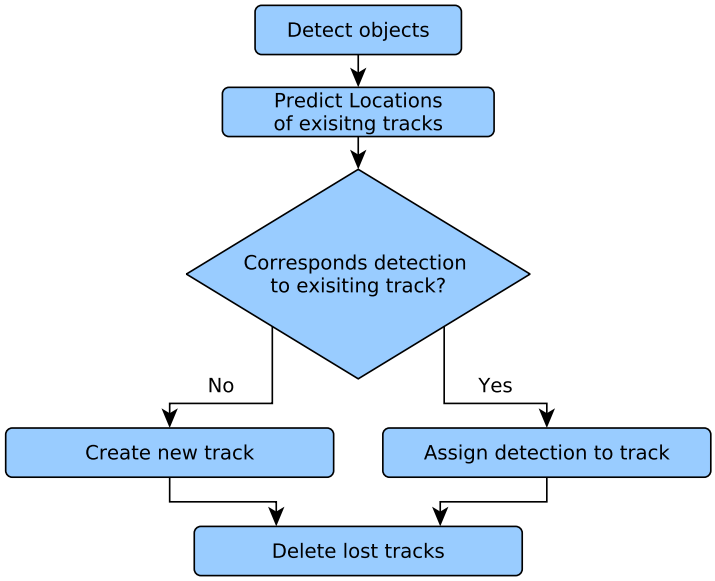

Figure 4.5.: Flow chart of the tracking algorithm.

For each image the calculated locations are saved to the track record. Each track has an identifier to distinguish between them. To solve the correspondence problem between frames a Kalman filter is used to predict the location in the consecutive frame. A Kalman filter is an algorithm that uses noisy measurement data over time to estimated the current state of a system. Therefore, it can be used to predict the current state of the system. A detailed explanation of the Kalman filter can be found in [38, 39]. Thereafter, an attempt is made to assign each detection in the succeeding frame to a predicted track. This is done via a cost function, where the cost increases with the distance from the predicted location and decreases with the confidence of the prediction by the Kalman filter. Also, a non-assignment has a certain cost, which effectively determines the

maximal distance between a predicted and a detected blob. If a predicted track has no corresponding detection it will be marked as invisible and deleted if no detection in the next 10 frames occurs. For detections which have no matching track a new track will be started.

If all frames of the sequences have been processed, the velocity can be inferred by taking the time derivative of the tracked locations. Due to the noisiness of the detections, that noise is amplified by simply taking the derivative. To avoid this behavior a Savitzky-Golay filter [40] is used, which utilises polynomials of a low degree to fit sub-sets of the data points by the method of linear least squares. The implementation used in this thesis can be called in Matlab by *sgolayfilt*. In this thesis a window width f of half the track length and degree of $k = \min(7, f/2)$ is used.

4.3 Synthetic sequences

To compare and evaluate the performance of different velocity detection algorithms it is mandatory to know the results beforehand. Several test cases have been designed to study the performance of different algorithms under controlled and realistic conditions. In the following, two methods of creating such sequences are explained and their advantages and limitations are discussed. The performance of the previously introduced velocity estimation algorithms is tested on these ground truth data and the results are presented in section 5.1.

4.3.1 Simple approach with exact positions

To verify sub-pixel accuracy of different algorithms, small displacements of heated dots need to be investigated. On a discrete grid, sub-pixel motions are reflected by small intensity changes of neighboring pixels (see fig. 4.6). Due to the discrete nature of images, it is only possible to spot these motions when the object of interest is resolved within several pixels of the image. Therefore, a two dimensional Gaussian distribution is cast onto an image filled with background with its center on a fraction of a pixel. The Gaussian intensity values have

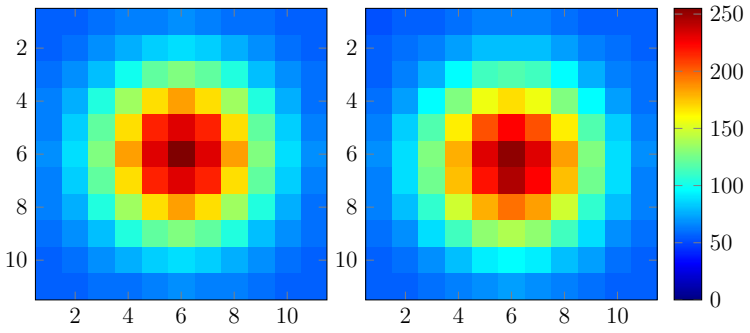

Figure 4.6.: Subpixel shift of 2D Gaussian by 0.25 pixels.

been sampled to the discrete grid of pixels by integrating over each pixel. The intensity value of each pixel $k_{x,y}$ becomes:

$$I_k(x,y) = \int_{k_x-\frac{1}{2}}^{k_x+\frac{1}{2}} \int_{k_y-\frac{1}{2}}^{k_y+\frac{1}{2}} I(x,y)dxdy \tag{4.29}$$

$$\text{with } I(x,y) = I_0 \exp\left(-\left(\frac{x-x_0}{r}\right)^2 - \left(\frac{y-y_0}{r}\right)^2\right), \tag{4.30}$$

where (x_0, y_0) denotes the location of the maximum and r the standard deviation of the two dimensional Gaussian distribution. Using the error function, one can calculate the intensity values for each pixel:

$$\text{erf}(x) = \frac{2}{\sqrt{\pi}} \int_0^x e^{-t^2} dt \tag{4.31}$$

Inserting and manipulating eq. (4.29) yields:

$$I_k = \frac{1}{4} I_0 \pi r^2 \cdot [\text{erf}(k_{x+}) - \text{erf}(k_{x-})] \cdot [\text{erf}(k_{y+}) - \text{erf}(k_{y-})] \tag{4.32}$$

$$\text{with } k_{x\pm} = k_x \pm \frac{1}{2} - x_0 \tag{4.33}$$

$$\text{and } k_{y\pm} = k_y \pm \frac{1}{2} - y_0. \tag{4.34}$$

These continuous values are rounded to the closest integer. It should be noted, that due to the limited bit size of 256 values for an 8-bit image, a lower boundary for the sub pixel resolution is created, which is $2^{-8} \approx 3.9 \times 10^{-3}$.

bit size	dx [px]
8	3.906×10^{-3}
16	1.526×10^{-5}
32	2.328×10^{-10}
64	5.421×10^{-20}

Table 4.1.: Results for the theoretical minimal possible shift, depending on bit size only

As one can see in Table 4.1 even 8 bit supports a fairly high accuracy, which will suffice for this thesis. Especially, if one considers noise in the image.
For each consecutive image the center of a Gaussian distribution can be specified and as a result a synthetic sequence with known location of the objects is generated and can be used for evaluating different algorithms.

4.3.2 Simulation of complex flow patterns

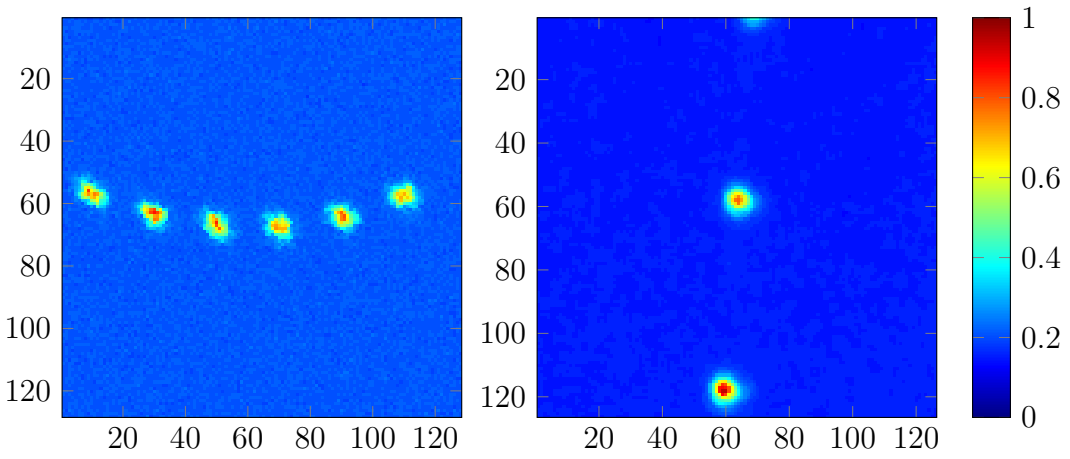

Figure 4.7.: Comparison of real with synthetic data (synthetic on the left).

To reflect the properties of a heat patch on a water surface more realistically, a more complex approach was investigated. The approach with exact location can not reflect that heated patches on a water surface undergo diffusion and shear stress, which will deform them remarkably. Instead of setting the center of the intensity distribution for each image of the sequence, a time dependent velocity field $\vec{v}(t)$ is specified. After the first image has been created (by the same means

as in section 4.3.1), each following image will be generated by applying this function:

$$I(x, y, t_{i+1}) = I(x - v_x(t+1), y - v_y(t+1), t_i) \tag{4.35}$$

This process is also known as inverse warping. The sequence can be controlled by applying velocity fields of arbitrary complexity. To cover a realistic range of flow patterns the following velocity fields were created and superimposed.

$$\begin{aligned} v_y &= A_p(R^2 - (x-R)^2) && \text{(Poiseuille flow)} \\ v_y &= A_w \sin(k_w y + \omega_w t) && \text{(Propagating waves)} \\ v_y &= A_s \sin(k_s x)^2 && \text{(Simulating streaks)} \end{aligned} \tag{4.36}$$

Additionally, noise has been applied to the velocity field to simulate diffusion in the x-y-plane, since diffusion is due to random motion. To accommodate for diffusion into the bulk, the intensity drops by a certain factor each frame. In fig. 4.7 the difference of actual data on the right and a synthetic image on the left is shown.

5

Results

In this chapter the velocities obtained from the synthetic image sequences as well as from the experimental data are presented. In the first section, the performance of the algorithms introduced in the last chapter will be evaluated by applying them to different synthetic and real data. Their accuracy and robustness will be evaluated. The second section presents the physical data and relates it to current models of transport processes of the air-sea interface.

5.1 Comparison of different algorithms for estimating surface velocities

As discussed in chapter 4, there are several possibilities to infer velocities from a given image sequence. To determine the best suited algorithm for detecting and measuring surface velocities, the above mentioned algorithms have been tested against artificially created as well as against real sequences from the Aeolotron.

Two different types of synthetic sequences have been developed. The first one explicitly enforces a heated spot with a Gaussian profile at a certain location for each frame, so $I_{\max}$ and the corresponding location is known. The locations are chosen in a way, that two types of motion were generated: one with constant velocity in y-direction from top to bottom and a sinusoidal movement along the y-axis. From the given locations the velocity is inferred. Therefore, it is possible to compare the algorithm's output against ground truth data. The second test case specifies the start positions of the intensity dots and calculates consecutive images from a time dependent velocity field, which were defined in section 4.3.2.

Since the real water surface is highly variable, the velocity estimation represents a challenging task. This two step approach is therefore ideal to investigate the behavior of each algorithm under increasing complexity. Due to the two different synthetic sequences, two goals are reached: the first sequence provides reliable ground truth data and the second method supplies a realistic test case to measure the performance of the algorithms under effects such as distortion and signal intensity decreasing with time, which also appear in real data sets taken from the Aeolotron. For the Aeolotron sequences there is no ground truth to compare against, instead a closer look is taken at the obtained data sets and the velocity distributions.

5.1.1 Location based Synthetic Sequences

The generated test sequences contain 100 frames with a resolution of 100x100 pixels at 8 bits. As explained in section 4.3.1, for each frame a Gaussian intensity distribution at a fixed position is given. Additionally, random noise has been added in varying degrees to examine the robustness of the algorithms (see eq. (3.1) for the definition of the SNR). Two different motions have been created, a constant motion with $v = 0.6\,\mathrm{px/frame}$ and a sinusoidal movement with a spatial amplitude of $A = 6.25\,\mathrm{px}$ and an angular frequency of $\omega = 0.1\,/\mathrm{frame}$.

In fig. 5.1 the estimated velocity is plotted against the frame number for the two types of motion. Some important characteristics of the different algorithms as well as some performance qualities are visible. For the constant motion, two

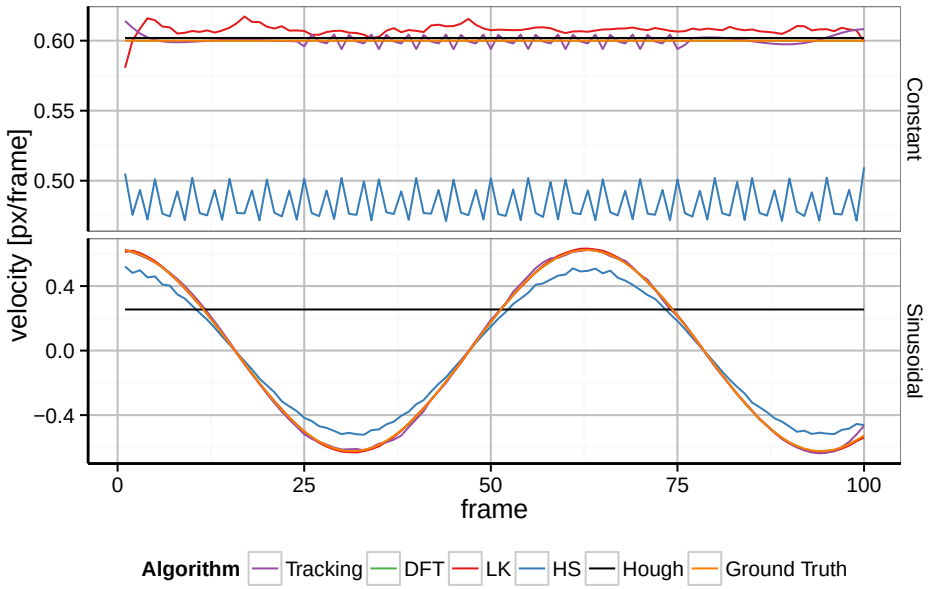

Figure 5.1.: Velocity vs frames for different algorithms, here with a SNR of 1000. The abbreviations used here are stated in section 4.2.

noticeable effects appear. The most obvious observation is that the optical flow algorithm based on Horn-Schunck underestimates the velocity by approximately 20%. This has two reasons: first, the Horn-Schunck algorithm has a global smoothness constraint, but in the sequences there is no global movement visible. Therefore, it smooths the velocity visible on the dot over the area where no movement is visible, hence decreasing the overall velocity. Second, the smoothness parameter α explained in section 4.2.2 is not optimized to the ground truth data, because no global minimum in the energy functional could be reached.

But also some other algorithms have problems in detecting the correct velocity. Another visible characteristic is the zigzag behavior of both optical flow algorithms – HS and LK – and of the tracking procedure. The zigzag lines of the tracking algorithm are due to smoothing artifacts from the Savitzky-Golay filter, which is applied to suppress the noise introduced by taking the derivative of the tracked positions. Since the Hough transform – in this implementation – can only detect straight lines and, therefore, is only able to evaluate constant velocities, it fails for sinusoidal motions.

As stated in section 4.2, the software frame work generates a track for each detected heated dot and appends all relevant properties to the track history. This also includes information about the velocity for each different algorithm. For each algorithm a separate vector

$$\mathbf{v}(t) = \begin{pmatrix} v_x(t) \\ v_y(t) \end{pmatrix} \tag{5.1}$$

containing the velocities is created.

To gauge the performance of each algorithm with numbers, the deviation from the ground truth is taken by

$$\mathrm{RMS} = \sqrt{\frac{1}{N}\sum_{i=1}^{N}(\mathbf{v}_i - \mathbf{v}_{i,\mathrm{true}})^2}, \tag{5.2}$$

where $\mathbf{v}_i$ is the velocity of the i-th frame derived from an algorithm of interest and $\mathbf{v}_{i,\mathrm{true}}$ is the known velocity, which is enforced by the synthetic sequence.

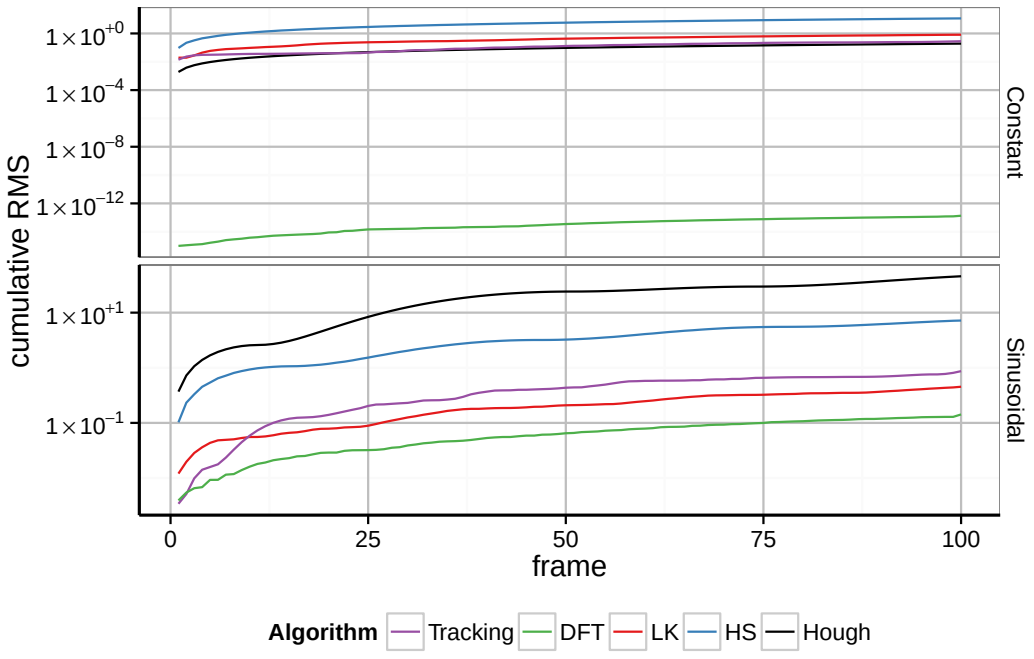

Figure 5.2.: RMS against frames for different algorithms using a signal to noise ratio of 1000.

In fig. 5.2 the cumulative RMS, which adds up over each frame is plotted for an SNR of 1000. In both motion setups the DFT algorithm is superior in terms of precision. Remarkable is the performance of the DFT for the constant motion which is 10 orders of magnitudes more accurate than the other methods.

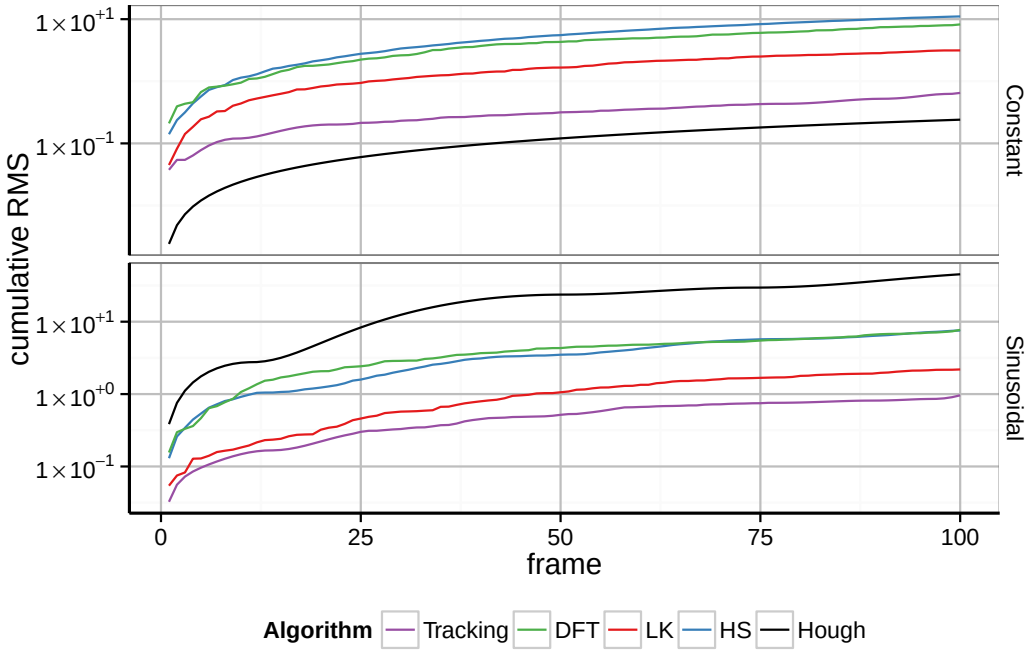

Figure 5.3.: RMS against frames for different algorithms. Now with a signal to noise ratio of 25.

This superiority ceases to exist when the noise intensifies, as can be seen in fig. 5.3. The overall best performance under a low SNR is delivered by the tracking algorithm and for constant motion the Hough approach yields the best result.

In fig. 5.4 the RMS plotted against the SNR is shown. Here it becomes evident that DFT and LK are highly affected by the SNR, while the other methods show a more stable behavior with varying SNR. Also, the orders of magnitudes superior performance of the DFT for the constant motion is put into perspective in this plot. In fig. 5.2 a SNR was chosen that is beneficial to the DFT. From the sinusoidal motion it becomes evident that the DFT is superior around a signal-to-noise-ratio of approximately 90.

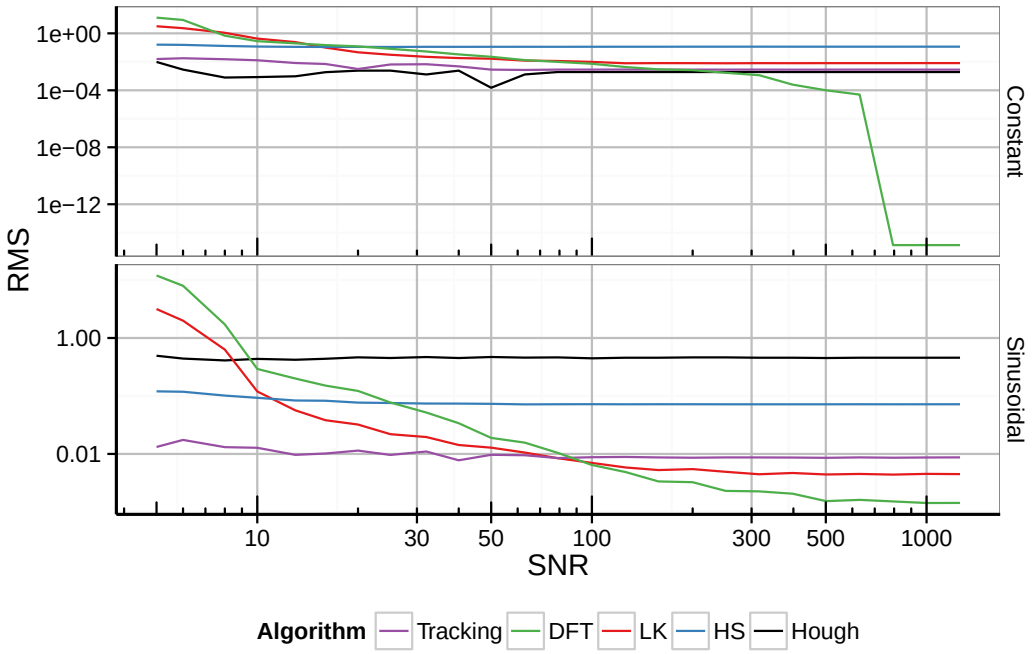

Figure 5.4.: RMS against SNR for different algorithms, for the location based synthetic sequences.

5.1.2 Flow Field based Synthetic Sequences

Since the Hough transform yields insufficient results for non-uniform motions it is omitted in the following. As stated in section 4.3.2 the sequences are generated by warping an initial image by a given space and time dependent velocity field (see eq. (4.36)). The image size is 128x128 pixels, 200 frames are generated. The dots are placed from $x = 10$ to $x = 110$ with an interval of $dx = 20$, all at the same y-position, $y = 10$, and have again a Gaussian profile with a diameter of 3 pixels. Values for the velocity field can be found in the appendix A.

In fig. 5.5 the relationship between the SNR and the RMS is shown for the velocity field based test sequence. One difference to the synthetic sequences used in section 5.1.1 is the better performance of the tracking approach especially in comparison with the DFT method. This difference is primarily due to the newly introduced possibility of the changing shape of the dots during the sequence. Hence, the normalized cross correlation – which is part of the DFT algorithm – is more likely to obtain inaccurate results. That is because the translated sub-image

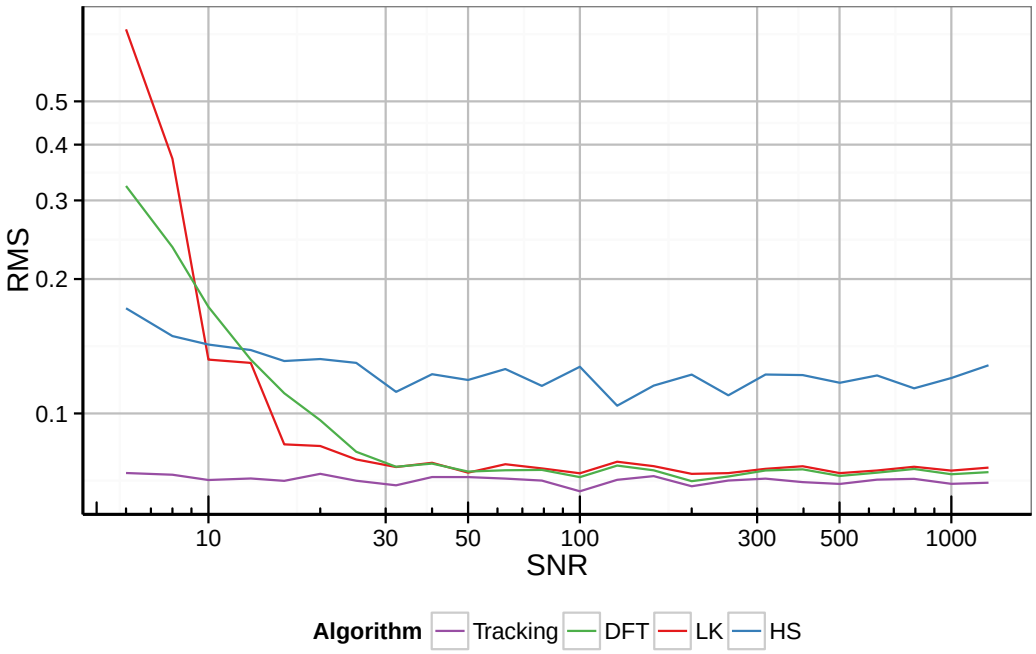

Figure 5.5.: RMS against SNR for different algorithms. The tracking algorithm performs best for all SNR.

does not match with the now distorted spot. In contrast, the tracking method uses the centroid of the detected blob which is more robust to shape deformation.

This behavior is also evident in fig. 5.6, where the accumulated error for each algorithm is shown. At the beginning of the sequence the DFT produces slightly better results for high SNR, but drops in accuracy pretty quickly, mainly due to the shape deformation.

Using the insights from this section, some algorithms can already be rejected. The Hough approach has been sorted out due to the inability to cope with non-uniform motion. Since the real water surface exhibits sinusoidal motions, the algorithm must prevail under a variable dot motion. Using the flow based synthetic sequences, were also the deformation of the heated dots was introduced, it becomes evident, that the DFT algorithm as well as the optical flow approach based on Lukas-Kanade are sensitive to shape distortions. The Horn-Schunck algorithm suffers under the sparse flow field, since only localized dots provide information about the velocity field. The tracking approach provides the best

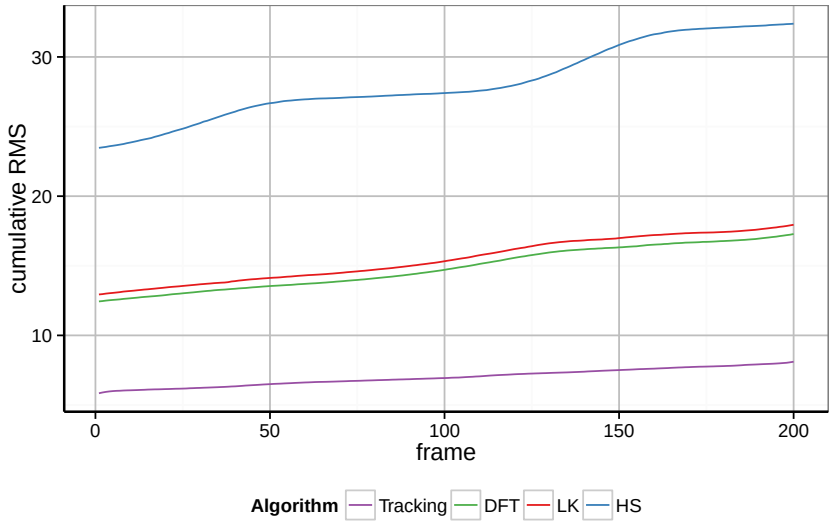

Figure 5.6.: Cumulative RMS over time for different algorithms (SNR = 50).

performance under the challenges of shape distortion and non-uniform motion. In the following, these findings are validated on real data sequences, considering only the DFT and the tracking approach.

5.1.3 Aeolotron Sequences

It becomes evident that not all algorithms are equally suited to be applied to the experimental data. The velocity field at the water surface leads to highly variable movements and distortions of the heated spot. In addition, the falling temperature of the dot leads to a decreasing SNR.

Since there is no ground truth for sequences taken in the Aeolotron, instead the overall consistency of the data is investigated. To make the following graphics clearer, only the DFT and the tracking algorithm are shown. Taking a closer look on the temporal behavior of the surface velocity in fig. 5.7 both algorithms in comparison are shown. Different symbols on the plot distinguish various tracks. In this plot it is evident that the DFT approach seems to underestimate the velocities is seen. Especially in the highlighted region – where newly detected tracks have their origin – the divergent development of both approaches. At the beginning of a track – when the SNR is still high – a good agreement between

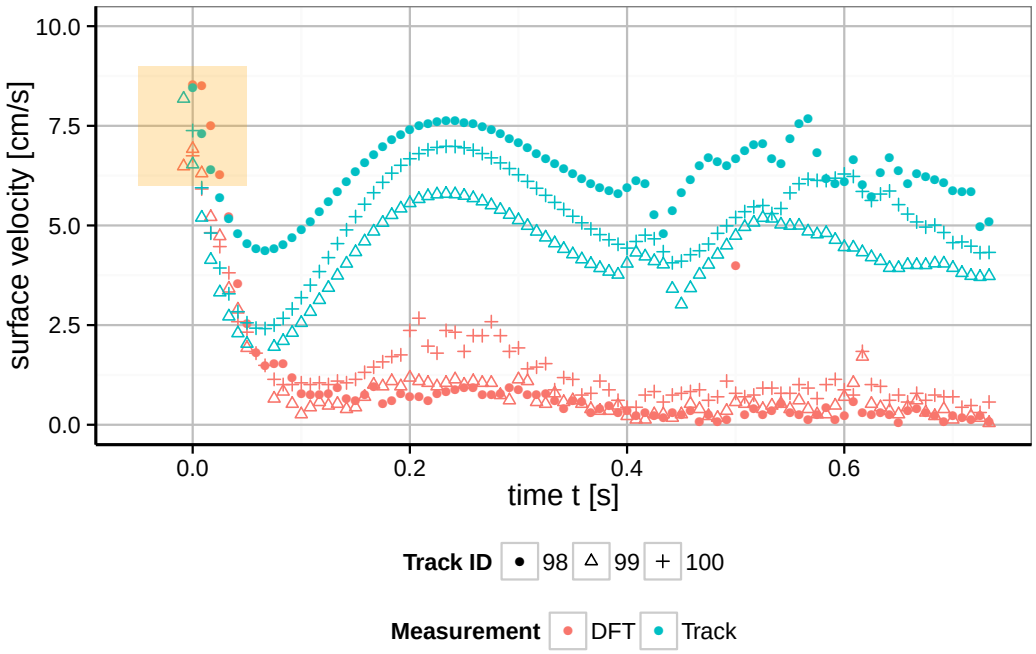

Figure 5.7.: Surface velocity plotted against time at a reference wind speed of $1.52\,\mathrm{m\,s^{-1}}$. The highlighted area marks the start of new detected tracks. The different symbols mark distinct tracks and the colors distinguish between both algorithms. It is recognizable, that the DFT method estimates a lower velocity, while the tracking algorithm shows clearly the modulation of the velocity due to the waves.

both approaches can be found, but around $t \approx 0.3\,\mathrm{s}$, the velocity stays below $2.5\,\mathrm{cm\,s^{-1}}$ for the DFT method. Since the DFT method underestimates the velocity in the presence of low SNR, the surface velocities in the following section are obtained by using the tracking approach. The other algorithms have been rejected due to their weaker performance in that specific setting of local heated dots on a highly variable water surface.

5.2 Surface Velocities

Considering the findings of section 5.1, where the tracking algorithm shows the best performance under low SNR, it is chosen as the standard algorithm for the following investigations. In fig. 5.8 the temporal evolution of the surface velocity

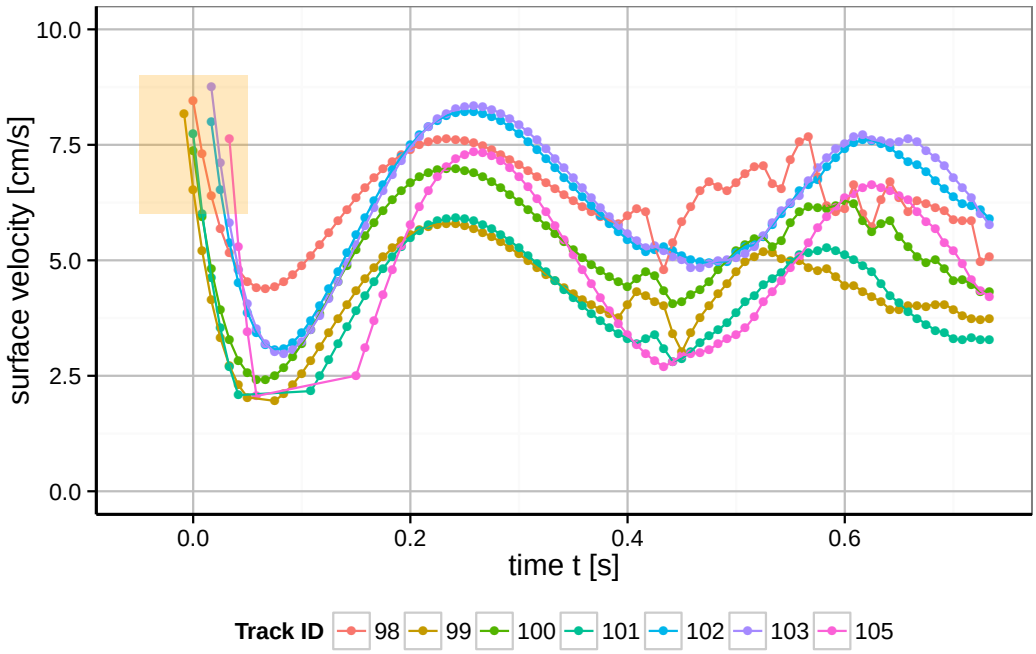

Figure 5.8.: Surface velocity plotted against time at a reference wind speed of $1.52\,\mathrm{m\,s^{-1}}$. The highlighted area marks the start of new detected tracks. Different colors mark distinct tracks of heated dots.

for several tracks in a time window of one second is shown. Seven new tracks are detected in the sequence. The general behavior shows a wave-like pattern, which is not surprising since even at reference wind speed of $1.52\,\mathrm{m\,s^{-1}}$ there are small wave amplitudes giving the impression of sinusoidal modulation of the velocity.

5.2.1 Velocity Distributions

In this section the velocity distributions of the surface are investigated at various wind wave conditions. Both surface and bulk velocities represent important quantities that describe the dynamic nature of the air sea boundary layer. From the difference between bulk and surface velocities important quantities of gas and/or momentum transfer can be derived.

5.2.2 Comparison of Surface Velocities and Bulk Velocities

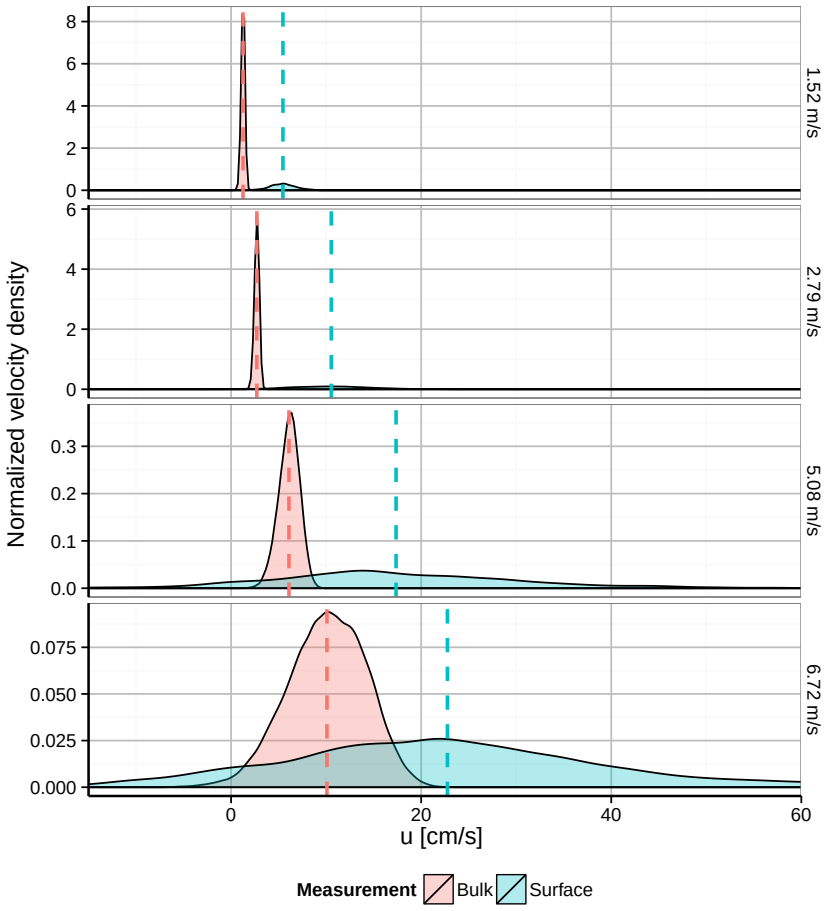

Figure 5.9.: Bulk and surface velocity distribution in comparison for different reference wind speeds. The dashed lines mark the mean of each velocity distribution. The distributions are normalized so that the area under curves is one.

Figure 5.9 gives an overview over the surface and the bulk velocity distributions (see section 3.3) for clean water conditions. The dashed line labels the mean surface velocity. It shows, that with increasing wind speed both distributions become broader and the mean shifts to higher velocities. The variation in surface velocities is much larger than for the bulk. This is not only due to the greater variety of speeds but also due to the following effect: when waves travel through the image and therefore lift the heated dot up or down, it can not be distinguished from a forwards or backwards motion. This issue and a possible solution is discussed in chapter 6. Another feature is the increasing difference

between the bulk and surface velocity with higher wind speeds which is also shown in fig. 5.10. These velocity differences allow insights into the mechanism at the boundary layer, which will be presented in the next section.

5.2.3 Momentum Transfer Resistance

u_{Surf} $[\mathrm{cm\,s^{-1}}]$	u_{Bulk} $[\mathrm{cm\,s^{-1}}]$	u_* $[\mathrm{cm\,s^{-1}}]$	u_{ref} $[\mathrm{m\,s^{-1}}]$	β	u_{10} $[\mathrm{m\,s^{-1}}]$
5.45	1.25	0.23	1.52	18.26	1.81
10.54	2.70	0.46	2.79	17.03	3.88
17.36	6.09	0.85	5.08	13.24	6.73
22.76	10.09	1.37	6.72	9.26	9.65

Table 5.1.: Values obtained for the measurements at the Aeolotron in April 2014. For the derived β values see eq. (5.5).

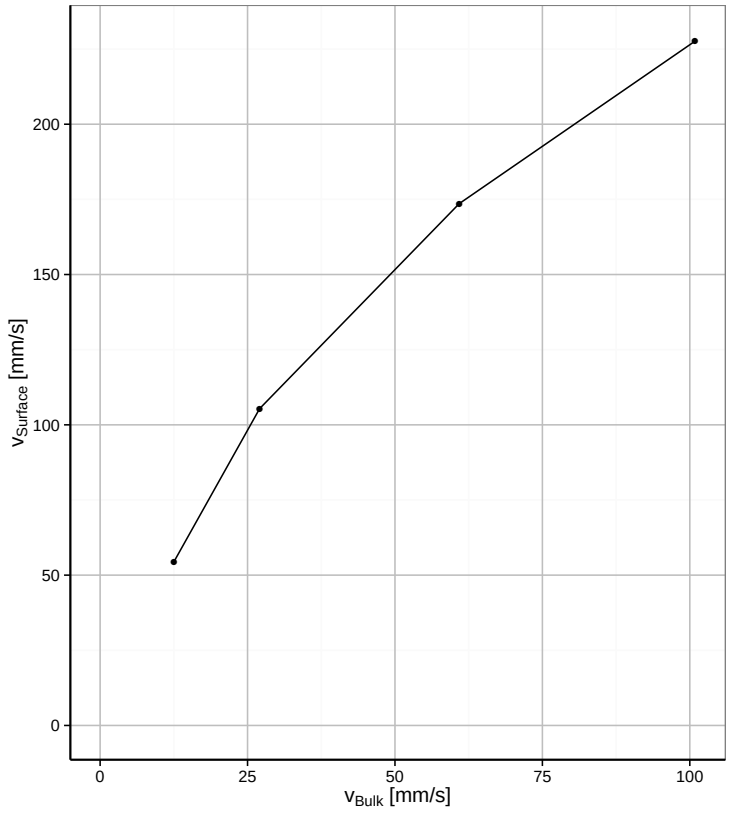

Figure 5.10.: Mean bulk against mean surface velocity.

In fig. 5.10 the relation of the bulk and surface velocity is shown. For increasing wind speeds the surface velocity increases less than the bulk velocity. One

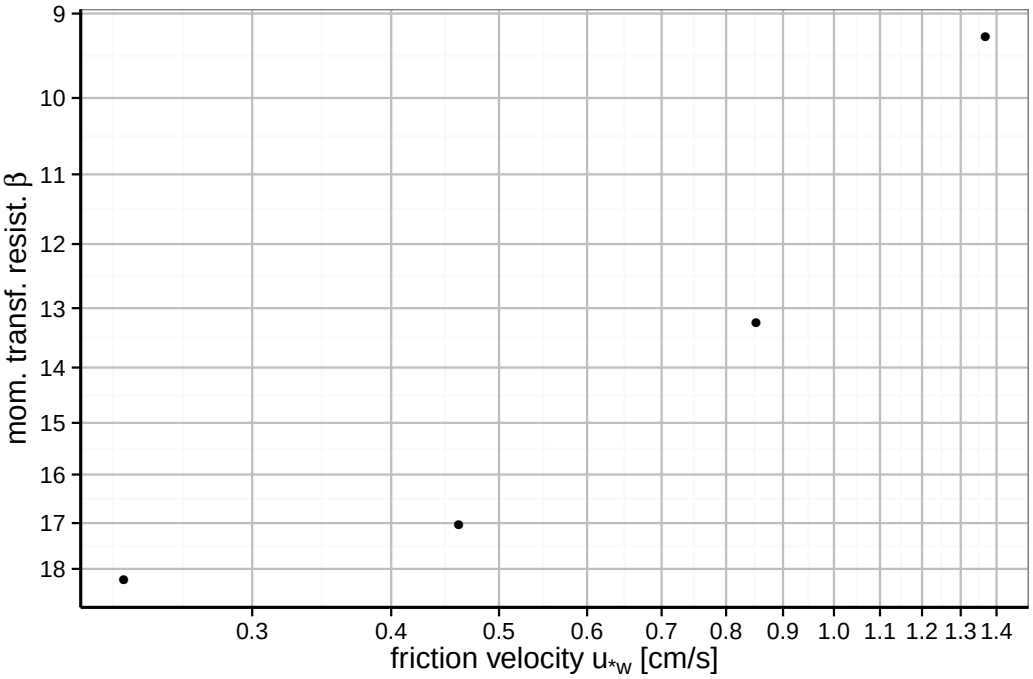

Figure 5.11.: Derived β values plotted against the water sided friction velocity. A decrease of β with growing u_* is clearly visible.

possible explanation lies in the process of wave formation. When waves start to develop, the shear stress tangential to the water surface decreases and the wave form drag increases. This leads to a drop in acceleration of the water surface.

As explained in section 2.1.3, the momentum transfer velocity can be parametrized by eq. (2.19). Combining eq. (2.19), the definition for the momentum transfer flux

$$\tau = k_m \Delta(\rho u) \tag{5.3}$$

and the definition of the friction velocity

$$u_* = \sqrt{\frac{\tau}{\rho}} \tag{5.4}$$

an expression for the momentum transfer resistance β can be found [41]:

$$\beta = \frac{\Delta u}{u_*}, \tag{5.5}$$

where Δu is the difference between the surface and the bulk velocity. This β is very important for the parametrization of exchange processes. It is a dimensionless constant which relates the gas and heat transfer velocities to the friction velocity, as stated in eq. (2.18). The values for the friction velocity are taken from experiments from [22] and are also depicted in table 5.1, while Δu is determined by the measured surface and bulk velocities. As stated in [22], the wind speed at the thermography site is increased by 15% and therefore, also the friction velocity. In fig. 5.11 β is plotted logarithmically against the friction velocity u_*. The overall picture of the data is in the expected order of magnitude ($\beta \approx 12.5$ for a smooth water surface [18, 42]). The small deviation to higher values for β could be explained by taking the form drag acting on the water surface into account, since $\beta \propto \frac{1}{u_*}$. It is noticeable, that with higher wind speeds the transfer resistance decreases. These findings differ from the ones made by [43] and [44] using gas exchange measurements. The measurement results from [44] have been extracted from a plot, since tabular values were not available. Measurements for the momentum transfer resistance were also derived by [45] with values for β in the range of 5-8 for low and 4-6 for high friction velocities.

These values were derived at a much smaller tank, and therefore, are not shown here. For a clean surface, experiments with N_2O and C_2HF_5 show an approximately constant behavior of β as can be seen in fig. 5.12. For measurements with surface films also a decrease in β is visible. The momentum transfer resistance β reported in [21] was calculated using

$$\beta = \frac{1}{k} u_* Sc^{-n} \tag{5.6}$$

from measured k, n and u_* which have measurement uncertainties. The uncertainty in n, as reported in [21] alone is in the order of 10–30 % which leads to the expectation of a large uncertainty in the estimation of beta.

This contradicting result produced in this thesis is rather unexpected and needs definitely further investigations. As stated in section 3.4, there are also some error sources. Even though, the experiments were carried out with clean water, surface films can still develop, if the water surface is not regularly skimmed. However, even taking additional surfactants into account, these large deviations between the differently obtained β values cannot be explained by surface films alone.

Another source of uncertainty is introduced by the measured bulk velocities. Since, the measurements are done in an annular facility, complex 3D flow fields develop. Therefore, the association of the measured bulk velocity to the surface velocity is at least precarious. Additionally, the assumption of a constant velocity throughout the bulk as described in section 2.1.2, is only a rough approximation.

The boundary layer at a free water surface and the interaction processes happening there remains a fascinating area of research and there are still some gaps in the knowledge of air-sea interactions, which need to be closed.

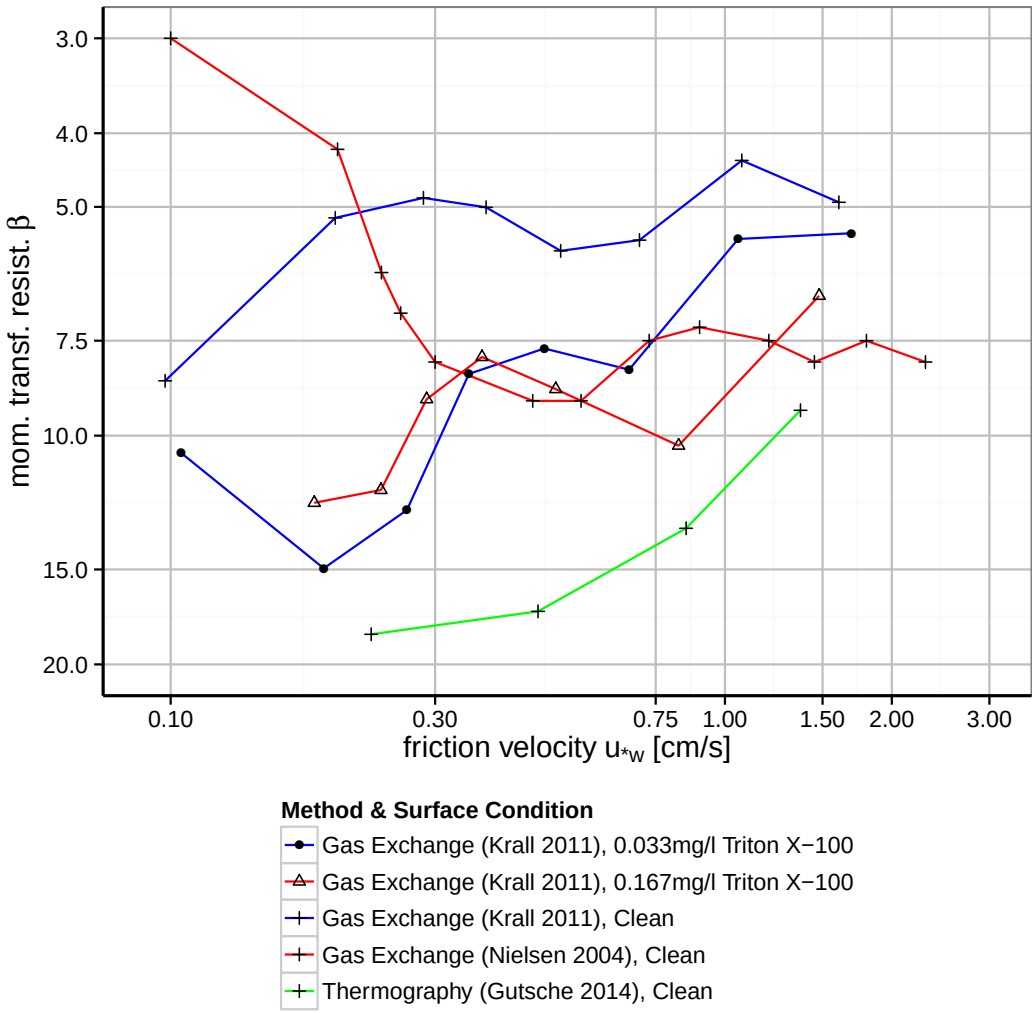

Figure 5.12.: Comparison of β values for different friction velocities obtained in this thesis and derived by [43] and [44] using gas exchange measurements.

6

Conclusions & Outlook

Investigating the transport processes at the air-sea interface remains a difficult and challenging problem. Understanding the exchange of heat and momentum in more detail is necessary to make accurate predictions about global scale climate changes. In this thesis surface and bulk velocities for different wind speeds by means of thermography have been measured. To select the best algorithm to determine the surface drift velocities from infrared images, under these special circumstances, synthetic sequences have been designed to compare different velocity estimation algorithms in a precisely controlled setup. It was found that for high signal-to-noise-ratios the cross correlation matching algorithm described in section 4.2.3 is best suited for this task, whereas the tracking methods presented in section 4.2.4 is superior under conditions with lower SNR. Both methods are on par for a SNR of approximately 90. Taking shape deformations into account, which are induced by shear currents, the performance of the DFT algorithm, which uses cross correlation matching, drops significantly.

The image sequences taken in the Aeolotron were analyzed with the tracking algorithm, since it provides the best results compared to other algorithms under a

highly variable water surface and decreasing intensity. These insights were helpful to reliably extract velocity information from measurements at the Aeolotron. The results show that with increasing wind speeds the surface velocity increases less than the bulk velocity. A plausible explanation is due to the energy needed to form waves, which have a greater surface energy than a flat surface. Using previously measured friction velocities, momentum transfer resistances have been derived. The obtained β values contradict previously conducted experiments which used chemical trace gases. This unexpected result requires further research to verify these findings and to clarify the suitability of the involved physical models.

Due to the 2D projection onto the camera sensor all 3D information is lost. Therefore, it is not possible to resolve the full 3D flow field. Other issues arise due to the motion of the waves, which cannot be completely distinguished from surface flow. To improve the accuracy and to study the behavior at the surface in more detail it would be beneficial to combine the thermography measurement technique with a 3D visualization method.

This could either be implemented as a stereo setup or a slope gauge combined with a height laser. Integrating over the wave slope yields a 3D reconstruction of the wave field [35], where the integration constant is given by the elevation measurement of the height laser [46]. An obvious advantage would be the possibility to distinguish between surface and wave motion i.e. between up-and-down and forward-backward motion. Another possibility which arises is the mapping between surface velocity and wave phase, allowing to distinguish between interaction processes at the wave crest and the trough.

Research is still needed in the area of the air-sea interactions as the results derived in this thesis show. Despite the difficulties in measuring accurate flow characteristics, it is worth to improve the efforts being made to solve the still remaining puzzles. The algorithms studied in this thesis in combination with the above mentioned wave and height measurements could contribute significantly to reach that goal.

A

Appendix

A.1 Used instruments

In this section the equipment which was used during the experiments at the Aeolotron is presented. The information are taken from the manufactures.

Carbon dioxide laser	
Manufacturer	Synrad, Inc.
Type	Evolution 100
Wave length	10.6 µm
Power output	10 W
Power stability	5%
Beam diameter	4 mm
Beam divergence	3.5 mrad
Polarization	linear, vertical

Table A.1.: Technical data of the used carbon dioxide laser. All data are information provided by the manufacturer.

Infrared camera	
Manufacturer	IRcam
Type	Velox 327K
Chip	Cadmium-Mercury-Telluride
Wave length range	3.4–5.0 µm
Resolution	640x521 pixels
Pixel pitch	24 µm
Max. frame rate (full)	207 Hz
Max. frame rate (partial image)	820 Hz
Integration time	50–12.75 µs
NEΔT	20 mK
A/D resolution	14 bit
Effective data rate	129.4 MB/s

Table A.2.: Technical data of the used infrared camera. All data are information provided by the manufacturer.

A.2 Flow field values

To create synthetic sequences resembling a realistic water surface, eq. (4.36) has been used

$$\begin{aligned} v_y &= A_p(R^2 - (x-R)^2) && \text{(Poiseuille flow)} \\ v_y &= A_w \sin(k_w y + \omega_w t) && \text{(Propagating waves)} \\ v_y &= A_s \sin(k_s x)^2 && \text{(Simulating streaks)} \end{aligned} \tag{A.1}$$

using the following parameters:

Parameter	Value
A_p	0.1 pixel/frame
R	64 pixel
A_w	0.4 pixel/frame
ω_w	0.05 /frame
k_w	0.5 /pixel
A_s	0.02 pixel/frame
k_s	3 /pixel

Table A.3.: Parameters used for the flow field based synthetic sequences.

Bibliography

[1] America's Climate Choices: Panel on Advancing the Science of Climate Change; National Research Council. *Advancing the Science of Climate Change*. The National Academies Press, 2010. ISBN: 9780309145886. URL: http://www.nap.edu/openbook.php?record_id=12782 (cit. on p. 1).

[2] Gordon Conway. "The science of climate change in Africa: impacts and adaptation". In: *Grantham Institute for Climate Change Discussion Paper* 1 (2009), p. 24 (cit. on p. 1).

[3] Paul J Durack, Susan E Wijffels, and Richard J Matear. "Ocean salinities reveal strong global water cycle intensification during 1950 to 2000". In: *science* 336.6080 (2012), pp. 455–458 (cit. on p. 1).

[4] IPCC. *Climate Change 2013: The Physical Science Basis. Contribution of Working Group I to the Fifth Assessment Report of the Intergovernmental Panel on Climate Change*. Ed. by T.F. Stocker et al. Cambridge, United Kingdom and New York, NY, USA: Cambridge University Press, 2013 (cit. on p. 1).

[5] Satoru Komori, Ryuichi Nagaosa, and Yasuhiro Murakami. "Turbulence structure and mass transfer across a sheared air–water interface in wind-driven turbulence". In: *Journal of Fluid Mechanics* 249 (1993), pp. 161–183 (cit. on p. 2).

[6] B Jähne et al. "Investigating the transfer processes across the free aqueous viscous boundary layer by the controlled flux method". In: *Tellus B* 41.2 (1989), pp. 177–195 (cit. on p. 2).

[7] Wu-ting Tsai et al. “Characteristics of interfacial signatures on a wind-driven gravity-capillary wave”. In: *Journal of Geophysical Research: Oceans* 118.4 (2013), pp. 1715–1735. ISSN: 2169-9291. DOI: 10.1002/jgrc.20145 (cit. on p. 2).

[8] W Kendall Melville, Fabrice Veron, and Christopher J White. “The velocity field under breaking waves: coherent structures and turbulence”. In: *Journal of Fluid Mechanics* 454 (2002), pp. 203–233 (cit. on p. 2).

[9] S. P. McKenna and W. R. McGillis. “Performance of digital image velocimetry processing techniques.” In: *ef* 32 (2002), p. 2 (cit. on p. 2).

[10] Christoph Garbe, Uwe Schimpf, and Bernd Jähne. “Measuring important parameters for air-sea heat exchange”. In: vol. 4710. 2002, pp. 171–182. DOI: 10.1117/12.459564 (cit. on p. 2).

[11] C. S. Garbe, K. Degreif, and B. Jähne. “Estimating the viscous shear stress at the water surface from active thermography”. In: *Transport at the Air Sea Interface — Measurements, Models and Parameterizations*. Ed. by C. S. Garbe, R. A. Handler, and B. Jähne. Berlin, Heidelberg: Springer-Verlag, 2007, pp. 223–239. DOI: 10.1007/978-3-540-36906-6_16 (cit. on p. 2).

[12] H. Schlichting and K. Gersten. *Grenzschicht-Theorie*. 10th ed. Heidelberg, Germany: Springer-Verlag, 2006 (cit. on pp. 3, 7).

[13] P. K. Kundu. *Fluid Mechanics*. 4th. San Diego, CA: Academic Press, Elsevier, 2008 (cit. on pp. 3, 7, 9).

[14] B. Jähne. “Zur Parametrisierung des Gasaustauschs mit Hilfe von Laborexperimenten”. IUP D-145, Link Nationalbibliothek http://d-nb.info/810123614. Dissertation. Institut für Umweltphysik, 1980. DOI: 10.5281/zenodo.10443. URL: http://www.ub.uni-heidelberg.de/archiv/16796 (cit. on p. 4).

[15] L. Prandtl. *Strömungslehre*. Vieweg, 1957 (cit. on p. 6).

[16] C. S. Garbe. “Measuring and Modeling Fluid Dynamic Processes using Digital Image Sequence Analysis”. Habilitation thesis. IWR, Fakultät für Physik und Astronomie, Univ. Heidelberg, 2007 (cit. on p. 8).

[17] E. L. Deacon. “Gas transfer to and across an air-water interface”. In: *tellus* 29 (1977), pp. 363–374. DOI: 10.1111/j.2153-3490.1977.tb00746.x (cit. on p. 8).

[18] B. Jähne et al. “On the parameters influencing air-water gas exchange”. In: *jgr* 92 (Feb. 1987), pp. 1937–1950. DOI: 10.1029/JC092iC02p01937 (cit. on pp. 8, 52).

[19] H. D. Downing and D. Williams. “Optical Constants of Water in the Infrared”. In: *jgr* 80.12 (1975), pp. 1656–1661 (cit. on p. 13).

[20] Maximilian Bopp and Bernd Jähne. “Measurements of the friction velocity in a circular wind-wave tank by the momentum balance method”. 2014 (cit. on pp. 16, 20).

[21] Kerstin Ellen Krall. “Laboratory Investigations of Air-Sea Gas Transfer under a Wide Range of Water Surface Conditions”. Dissertation. Institut für Umweltphysik, Fakultät für Physik und Astronomie, Univ. Heidelberg, 2013 (cit. on pp. 16, 52).

[22] Maximilian Bopp. “Luft- und wasserseitige Strömungsverhältnisse im ringförmigen Heidelberger Wind-Wellen-Kanal (Aeolotron)”. Masterarbeit. Institut für Umwelphysik, Univeristät Heidelberg, Germany, 2014. URL: http://www.ub.uni-heidelberg.de/archiv/16962 (cit. on pp. 16, 52).

[23] M. Bopp. “Messung der Schubspannungsgeschwindigkeit am Heidelberger Aeolotron mittels der Impulsbilanzmethode”. Bachelor thesis. Institut für Umweltphysik, Fakultät für Physik und Astronomie, Univ. Heidelberg, 2011 (cit. on p. 19).

[24] James B. Edson et al. “On the exchange of momentum over the open ocean”. In: *jpo* 43 (2013), pp. 1589–1610. DOI: 10.1175/JPO-D-12-0173.1 (cit. on p. 20).

[25] Nobuyuki Otsu. “A threshold selection method from gray-level histograms”. In: *Automatica* 11.285-296 (1975), pp. 23–27 (cit. on p. 22).

[26] Mehmet Sezgin et al. “Survey over image thresholding techniques and quantitative performance evaluation”. In: *Journal of Electronic imaging* 13.1 (2004), pp. 146–168 (cit. on p. 22).

[27] Bernd Jähne. *Digital Image Processing*. 6th ed. Berlin: Springer, 2005. DOI: 10.1007/3-540-27563-0 (cit. on pp. 22, 26).

[28] Jordi Freixenet et al. “Yet another survey on image segmentation: Region and boundary information integration”. In: *Computer Vision—ECCV 2002*. Springer, 2002, pp. 408–422 (cit. on p. 22).

[29] D-S Lee. “Effective Gaussian mixture learning for video background subtraction”. In: *Pattern Analysis and Machine Intelligence, IEEE Transactions on* 27.5 (2005), pp. 827–832 (cit. on p. 22).

[30] John Canny. “A computational approach to edge detection”. In: *Pattern Analysis and Machine Intelligence, IEEE Transactions on* 6 (1986), pp. 679–698 (cit. on p. 23).

[31] Hanan Samet and Markku Tamminen. “Efficient component labeling of images of arbitrary dimension represented by linear bintrees”. In: *Pattern Analysis and Machine Intelligence, IEEE Transactions on* 10.4 (1988), pp. 579–586 (cit. on p. 24).

[32] Michael B Dillencourt, Hanan Samet, and Markku Tamminen. “A general approach to connected-component labeling for arbitrary image representations”. In: *Journal of the ACM (JACM)* 39.2 (1992), pp. 253–280 (cit. on p. 24).

[33] Paul VC Hough. *Method and means for recognizing complex patterns*. US Patent 3,069,654. 1962 (cit. on p. 25).

[34] B. K. P. Horn and B. Schunk. “Determining Optical Flow”. In: *Artificial Intelligence* 17 (1981), pp. 185–204 (cit. on p. 28).

[35] Daniel Kiefhaber. “Optical Measurement of Short Wind Waves — from the Laboratory to the Field”. Dissertation. Institut für Umweltphysik, Fakultät für Physik und Astronomie, Univ. Heidelberg, 2014. URL: http://www.ub.uni-heidelberg.de/archiv/16304 (cit. on pp. 32, 33, 56).

[36] Manuel Guizar-Sicairos, Samuel T Thurman, and James R Fienup. “Efficient subpixel image registration algorithms”. In: *Optics letters* 33.2 (2008), pp. 156–158 (cit. on p. 32).

[37] Inc. The MathWorks. *Motion-Based Multiple Object Tracking*. June 2014. URL: http://www.mathworks.de/de/help/vision/examples/motion-based-multiple-object-tracking.html (cit. on p. 33).

[38] Marcel Gutsche. “Playing soccer with the humanoid robot NAO”. Masterarbeit. Interdisciplinary Center for Scientific Computing (IWR) in Heidelberg, Germany, 2012. URL: http://www.ub.uni-heidelberg.de/archiv/16962 (cit. on p. 34).

[39] Rudolph Emil Kalman. “A new approach to linear filtering and prediction problems”. In: *Journal of Fluids Engineering* 82.1 (1960), pp. 35–45 (cit. on p. 34).

[40] Abraham Savitzky and Marcel JE Golay. “Smoothing and differentiation of data by simplified least squares procedures.” In: *Analytical chemistry* 36.8 (1964), pp. 1627–1639 (cit. on p. 35).

[41] C. Kräuter Kerstin E. Krall and Bernd Jähne. “Air-Sea gas exchange and momentum transfer: turbulence resistance in the viscous boundary layer and the Schmidt number dependency”. 2014 (cit. on p. 51).

[42] M. Coantic. “A model of gas transfer across air–water interfaces with capillary waves”. In: 91 (1986), pp. 3925–3943. DOI: 10.1029/JC091iC03p03925 (cit. on p. 52).

[43] Kerstin E. Krall and Bernd Jähne. “Air-Sea Gas Exchange and Momentum Transfer: Turbulence and Schmidt Number Dependency”. 2014 (cit. on pp. 52, 53).

[44] R. Nielsen. “Gasaustausch - Entwicklung und Ergebnis eines schnellen Massenbilanzverfahrens zur Messung der Austauschparameter”. Dissertation. Institut für Umweltphysik, Fakultät für Physik und Astronomie, Univ. Heidelberg, 2004. URL: http://www.ub.uni-heidelberg.de/archiv/5032 (cit. on pp. 52, 53).

[45] K. Degreif. “Untersuchungen zum Gasaustausch - Entwicklung und Applikation eines zeitlich aufgelösten Massenbilanzverfahrens”. Dissertation. Institut für Umweltphysik, Fakultät für Physik und Astronomie, Univ. Heidelberg, 2006. URL: http://www.ub.uni-heidelberg.de/archiv/6120 (cit. on p. 52).

[46] Jason Horn. “Hochaufgelöste optische Wellenhöhenmessung am Aeolotron mit Laser-induzierter Fluoreszenz”. Bachelorarbeit. Institut für Umwelphysik, Univeristät Heidelberg, Germany, 2013 (cit. on p. 56).

List of Figures

Danksagung

An dieser Stelle möchte ich mich ganz herzlich bei all denen bedanken, die mich bei dieser Arbeit unterstützt haben.

Mein besondere Dank geht an Prof. Dr. Bernd Jähne, der es mir ermöglicht hat in seiner Arbeitsgruppe an diesem spannenden Thema zu arbeiten und immer hilfreiches Feedback liefern konnte. Auch vielen Dank an PD Dr. Christoph Garbe, der sich freundlicherweise dafür bereit erklärt hat die Zweitbegutachtung durchzuführen.

Außerdem möchte ich der gesamten *Windis*-Arbeitsgruppe für die tolle Arbeitsatmosphäre und die immer hilfreichen Gespräche danken. Insbesondere möchte ich folgende Personen erwähnen:

Dr. Leila Nagel gebührt mein Dank für die kompetente Einführung in die Thermographie und die schnelle Hilfe bei allen technischen Problemen. Jana Schnieders danke ich für die stets hilfreichen Informationen bezüglich der Geschwindigkeitsschätzalgorithmen und für die tatkräftige Unterstützung bei nächtlichen Messungen. Bei Dr. Kerstin Krall bedanke ich mich für die Bereitstellung der Gasaustauschdaten. Max Bopp danke ich für die Zurverfügungstellung der u_* Werte. Jakob Kunz danke ich für die Hilfe bei vielen Arbeiten am Messaufbau.

Erklärung

Ich versichere, dass ich diese Arbeit selbstständig verfasst und keine anderen als die angegebenen Quellen und Hilfsmittel benutzt habe.

Heidelberg, den 1. August 2014,